EXPLOITING SECOND HARMONIC GENERATION FOR MICROELECTRONICS INTERFACE CHARACTERIZATION

A Thesis Submitted to
the Graduate School of Engineering and Sciences of
İzmir Institute of Technology
in Partial Fulfillment of the Requirements for the Degree of

MASTER OF SCIENCE

in Electrical and Electronics Engineering

by
Gizem SOYLU

May 2016
İZMİR

We approve the thesis of **Gizem SOYLU**

Examining Committee Members:

_____

Prof. Dr. Mehmet Salih DİNLEYİCİ
Department of Electrical and Electronics Engineering, Izmir Institute of Technology

_____

Assoc. Prof. Dr. Serkan ATEŞ
Department of Physics, Izmir Institute of Technology

_____

Assoc. Prof. Dr. Metin Hüseyin SABUNCU
Department of Electrical and Electronics Engineering, Dokuz Eylul University

_____

Assist. Prof. Dr. Kıvılcım Yüksel ALDOĞAN
Department of Electrical and Electronics Engineering, Izmir Institute of Technology

_____

Assist. Prof. Dr. Fatih YAMAN
Department of Electrical and Electronics Engineering, Izmir Institute of Technology

30 May 2016

_____

Prof. Dr. Mehmet Salih DİNLEYİCİ
Supervisor, Department of Electrical Electronics Engineering,
Izmir Institute of Technology

_____

Assist. Prof. Dr. Kıvılcım Yüksel ALDOĞAN
Co-Supervisor, Department of Electrical and and Electronics Engineering, Izmir Institute of Technology

_____

Prof. Dr. Mehmet Salih DİNLEYİCİ
Head of the Department of Electrical and Electronics Engineering

_____

Prof. Dr. Bilge KARAÇALI
Dean of the Graduated School Engineering and Sciences

ACKNOWLEDGEMENTS

Firstly, I would like to express my sincere gratitude to my advisor Prof. Mehmet Salih DİNLEYİCİ for support of my master thesis, his motivation, immense knowledge and valuable advice on this thesis. The completion of my research would not have been accomplished without his support. Secondly, I would like to thank my co-advisor Assist. Prof. Dr. Kıvılcım Yüksel ALDOĞAN for understanding, guidance and support through this study.

I would like to thank Guy VİTRANT for giving me the opportunity to work IMEP-LAHC laboratory. He has been such a pattern to me as a scientist, and I really appreciate all his support and encouragement during my master project. I also would like to thank the rest of SHG team during my internship in Grenoble, France: Irina IONICA, Luca PIRRO, Dimitrios DAMIANOS, John CHANGALA, Anne KAMINSKI and Sorin CRISTOLOVEANU for their encouragement, inspiring discussion and help. I am very proud that I had the chance to work with them.

I am also grateful to Çağın EKİCİ and Göksenin BOZDAĞ for their unfailing encouragement. Without their friendship, support and discussion about physics, the days in the lab would have been so pleasant. I would like to thank Tuğçe SEMERCİ for being great friend and always supporting me, and also thank Nurhan ARSLAN for her support and friendship during master studies. I wish them all best in their future endeavors.

Last but not least, I would like to express immense appreciation and thanks my mother Leyla SOYLU, my father Rüknettin SOYLU and my brother Meriç Can SOYLU for their unending love, sacrifice and unconditional support.

ABSTRACT

EXPLOITING SECOND HARMONIC GENERATION FOR MICROELECTRONICS INTERFACE CHARACTERIZATION

This thesis aims to develop a technique to characterize microelectronic interfaces based on Second Harmonic Generation (SHG) method. In the experiment part of this study, silicon wafers with thermal and native oxide, silicon-on-insulator (SOI), pure glass and glass with TiO_2 thin film samples were used to observe Second Harmonic (SH) signal. The experiments have been performed in IMEP-LAHC laboratory in Grenoble, France. In addition, the measurements were carried out with "Harmonic F1X" which is a femtosecond laser developed by the company FemtoMetrix based in California/USA (FemtoMetrix). Three contributions to SHG were investigated experimentally: the electric dipole approximation due to symmetry breaking at the surface/interface, a dc electric field because of the charge separation at the interface, and lastly bulk contributions. Then, the phenomenological model of surface SHG (Mizrahi & Sipe, 1988) was simulated in MATLAB, and the ratios of the elements of second order nonlinear susceptibility (χ_{zzz}/χ_{zii} and χ_{izi}/χ_{zii}) for the silicon wafers were identified with comparing the model with the experimental results. In addition, it was shown that surface and bulk contributions can be separated by using specific polarization states and azimuthal orientations. To show this separation, Fourier coefficients, which describes the crystal facial orientations of the total SHG, were determined for the silicon wafers. Furthermore, it was observed that there are some critical parameters which have an effect to SHG: the polarization states of the incident light and second harmonic light, the angle of incidence of the incoming light and the oxidation types of silicon. Finally, SOI has been used to check whether the effecting factors are same for silicon wafers. The findings demonstrate that SHG is a powerful technique to characterize the surface/interface and the bulk of the sample in microelectronic industry.

ÖZET

İKİNCİ HARMONİK JENERASYON YÖNTEMİ İLE MİKROELEKTRONİK ARAYÜZLERİN KARAKTERİZE EDİLMESİ

Bu tez ikinci harmonik jenerasyon (SHG) metodunu temel alarak mikroelektronik arayüzleri karakterize etmek için bir teknik geliştirmeyi amaçlamaktadır. Bu çalışmanın deneysel kısımda, ikinci harmonik (SH) sinyali gözlemlemek için termal ve doğal oksitlenmiş silikon plakalar, yalıtkan üstü silikon (SOI), katıksız cam ve TiO_2 ince film kalplı cam kullanıldı. Deneyler Fransa'nın Grenoble şehrinde IMEP-LAHC laboratuarında yapıldı. Bununla beraber, ölçümler Amerika'nın California eyaletinde bulunan FemtoMetrix adlı bir şirket tarafından geliştirilen bir femtosaniye lazer olan 'Harmonic F1X' ile gerçekleştirildi (FemtoMetrix). SHG'yi oluşturan üç katkı deneysel olarak incelendi: yüzey/arayüzey simetri kırılmalarından oluşan elektrik dipol yaklaşımı, arayüzeydeki yüklerin birbirlerinden ayrılmasından oluşan dc elektrik alanı ve son olarak yığından gelen katkılar. Yüzey SHG'si için fenomenolojik model (Mizrahi & Sipe, 1988) MATLAB'da simüle edildi, ve doğrusal olmayan ikinci dereceden suseptibilitenin elemanlarının oranları (χ_{zzz}/χ_{zii} ve χ_{izi}/χ_{zii}) model ve deneysel sonuçlar karşılaştırılarak silikon plakalar için belirlendi. Ayrıca, yüzey ve yığın katkılarının belli polarizasyon durumları ve azimuthal oryantasyonları kullanılarak ayrılabileceği gösterildi. Bu ayrımı gösterebilmek için, kristalin bütün ikinci harmonik jenerasyonunu oluşturan yüzey oryentasyonlarını tanımlayan Fourier katsayıları, silikon plakalar için bulundu. Bununla beraber, ikinci harmonik jenerasyonu etkileyen bazı kritik parametreler bulundu: gelen ışığın ve ikinci harmonik ışığın polarizasyon durumları, gelen ışığın gelme açısı ve silikonun oksitlenme türleri. Son olarak, silikon plakalara etki eden farktörlerin aynı olup olmadığını karşılaştırmak için SOI kullanıldı. Bulunan sonuçlar gösteriyor ki mikroelektronik endüstrisinde ikinci harmonik jenerasyon malzemenin yüzey/arayüz ve yığınını karakterize etmek için etkili bir teknik olduğunu ortaya koymaktadır.

TABLE OF CONTENTS

LIST OF FIGURES

Figure **Page**

LIST OF TABLES

Table **Page**

CHAPTER 1

INTRODUCTION

Optical Second Harmonic Generation (SHG) was discovered in a centrosymmetric quartz crystal by Franken et al. in 1961 (Franken et al., 1961) after the invention of the first laser by Maiman in 1960. In their experiment, which was also the first experiment of the nonlinear optics, they propagated a ruby laser beam with a wavelength of 694.3 nm through a centrosymmetric quartz crystal and observed the SHG signal at the wavelength of 347.15 nm from the crystal. Afterwards, second harmonic phenomenological theories were developed for different materials including semiconductor (Bloembergen et al., 1968) and dielectric solids (Wang and Duminski, 1968). Afterwards in 1970s, relatively little research was done. However, the end of 1980s, with the discovery of Ti:sapphire laser, spectroscopic SHG studies saw a renewed interest especially in device technology and in microelectronics industry.

1.1. Second Harmonic Generation as a Characterization Method

There is always a need for better control of semiconductor's surfaces and bulk in microelectronics industry. The nonlinear optical techniques of second harmonic generation is a promising way to characterize the quality and the structures of these materials thanks to non-destructive and contactless features (Kwon, 2006).

The theory behind SHG arises from the second or higher order nonlinear susceptibility $\left(\chi^{(n)}\right)$ of the material. As shown in Figure 1.1, the atoms are arranged in a centrosymmetric material, and SHG is forbidden in the bulk because of the inversion symmetry. However, this symmetry is broken at the surface region and it gives rise to electric dipole contribution to SHG. Therefore, SHG's strong sensitivity to surfaces and interfaces root in the presence of the broken inversion symmetry. This advantage of SHG can be used to access the interface between two mediums if the top medium is transparent such as SiO_2.

In addition, time-resolved second harmonic generation is used to study the charge carrier dynamics in semiconductors's interface regions. It is known as Electric Field

Induced Second Harmonic Generation (EFISH). This approach gives information about trapping, de-trapping and carrier injection in thin film layers of semiconductor devices. It is very important advantage of using SHG method because it is almost impossible to obtain these behaviors using conventional electrical measurements. As an example, it has been observed that silicon wafers with thermal and native oxide have different saturation periods in this study.

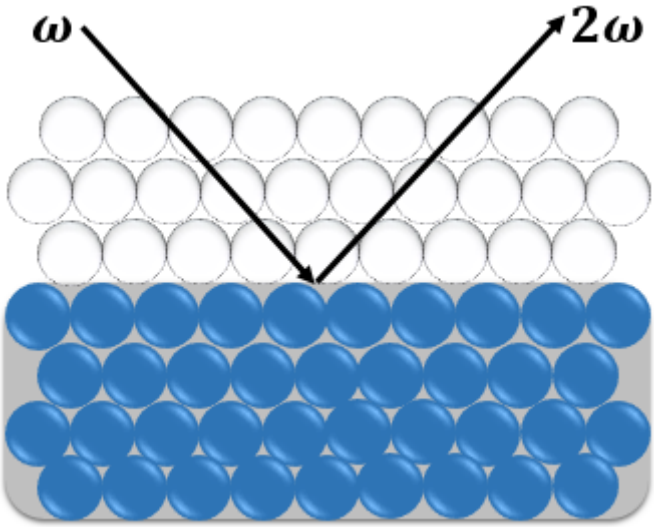

Figure 1.1. The inversion symmetry is broken just the surface of the sample

In the bulk of centrosymmetric media such as crystal Si, SHG is forbidden within electric dipole approximation. However, only higher-order contribution, which are magnetic dipole and electric quadrupole effect, can generate second harmonic (SH) light. In addition, the SHG response depends on the crystal structure of the material. If the crystal is rotated about its surface normal, the crystal structure of bulk can be identified. Also, this optical anisotropic behavior is used to distinguish the isotropic surface contribution and anisotropic bulk contribution. In the experimental part of this thesis, these contributions have been determined by using truncated Fourier expansion and shown the crystal structure of silicon wafers and Silicon on Insulator (SOI).

Among the many works of nonlinear optics, second harmonic generation plays an essential role. As a result, SHG is very effective technique to characterize interfaces and can be used to investigate in strain (Govorkov et al., 1990; Shriever et al., 2010), radiation induced defects (Marka et al., 2000; Pasternak et al., 2003), metalic contamination (Alles et al., 2007), roughness (Dadap et al., 1994), interface electric field (Luppi et al., 2010), crystal orientation (Tom et al., 1983) and miscuts (Lüpke et al., 1993).

1.2. Thesis Outline

This thesis presents how second harmonic light can be generated in a nonlinear material and how it can be used as a characterization method in microelectronics. There are three parts which compose of this study: the theoretical background of SHG, the experimental setup and lastly the experimental and simulation results of SHG.

Chapter 2 presents the theoretical part of SHG. Firstly, it focuses on different effects at the origin of second harmonic light generated from the interface, the static electric field near the interface and the bulk. These three contributions are described and formulized in different parts of chapter 2. In addition, some previous work is showed to compare our experimental results later.

Chapter 3 shows the experimental setup of "Harmonic F1X" which is a commercial equipment. This chapter describes the working principle, the properties of the laser and the experimental parameters of this machine.

In the work presented in Chapter 4, we investigate which parameters have an influence on the SHG intensity. Our experimental results are performed for Si(100) wafers and SOI. We explain our results according to angle of incidence light, the polarization angles of laser and detector, the azimuthal angle of sample, and the oxidation types of silicon and time dependency of second harmonic light. In the simulation model, we identified the ratios of the elements of second order nonlinear susceptibility and determined the Fourier coefficients which shows the different contributions come from the interface and the bulk of the materials.

At the end of the thesis, Chapter 5 summarizes all works which we have done in this study and discusses about the experimental and simulation results.

CHAPTER 2

THEORETICAL BACKGROUND OF SECOND HARMONIC GENERATION

The response of the medium in the optical system can be described by the induced polarization. In linear optics, the polarization $\mathbf{P}(t)$ is directly proportional to the electric filed $\mathbf{E}(t)$ and it can be expressed as

$$\mathbf{P}(t) = \epsilon_0 \chi^{(1)} \mathbf{E}(t) \tag{2.1}$$

where the constant of $\chi^{(1)}$ is defined as the linear susceptibility tensor and ϵ_0 is the permittivity of free space. Necessarily, the electric field and the induced polarization have the same frequency in linear optics. However, when the incident light is very intense, electrons vibrations is unharmonic (Kwon, 2006). Because of this light matter interaction, the light which is generated by the induced polarization, either in transmission or in reflection, will contain harmonics of the exciting light frequency. At this high intensity, the induced electric polarization is driven into the nonlinear regime and can be expanded in power series of the electric field $\mathbf{E}(t)$;

$$\begin{aligned} \mathbf{P}(t) &= \epsilon_0 \left[\chi^{(1)} \mathbf{E}(t) + \chi^{(2)} \mathbf{E^2}(t) + \chi^{(3)} \mathbf{E^3}(t) + \cdots \right] \\ &= \mathbf{P^{(1)}}(t) + \mathbf{P^{(2)}}(t) + \mathbf{P^{(3)}}(t) + \cdots \end{aligned} \tag{2.2}$$

where $\chi^{(n)}$ is the n^{th} order susceptibility and is a tensor of rank n+1. Second- and third-order nonlinear polarization can be denoted as $\mathbf{P^{(2)}}(t)$ and $\mathbf{P^{(3)}}(t)$. The second harmonic light is generated from the incident light. The intensity of second harmonic light is proportional to the square of the intensity of the incident light (Park, 2010),

$$I(2\omega) \propto \left| \mathbf{P^{(2)}} \right|^2 = \left| \chi^{(2)} \mathbf{E^2}(\omega) \right|^2 = \left| \chi^{(2)} \right|^2 I(\omega)^2 \tag{2.3}$$

There are three contributions to the SHG signal (Aktsipetrov et al., 1996): the surface dipole contribution, the bulk quadrupole contribution and a third one through $\chi^{(3)}$ in the case of the presence of a static electric field (EFISH). The nonlinear second-order total polarization at 2ω frequency can be modeled by (Gielis et al., 2008; Sipe et al., 1987)

$$\mathbf{P}_{\text{total}}^{2\omega} = \mathbf{P}_{\text{Surface}}^{2\omega} + \mathbf{P}_{\text{bulk}}^{2\omega} + \mathbf{P}_{\text{efish}}^{2\omega} \tag{2.4}$$

where $\mathbf{P}_{\text{Surface}}^{2\omega}$ is the surface polarization, $\mathbf{P}_{\text{bulk}}^{2\omega}$ is the bulk quadrupole polarization and lastly $\mathbf{P}_{\text{efish}}^{2\omega}$ is the dc-electric-field-induced polarization. One of the main important feature of SHG is that SHG is equal to zero for centrosymmetric materials and can only exists in the case of a non-centrosymmetric ones (Boyd, 2007). The first mentioned effect (surface) is due to symmetry breaking at the surface and concerns atoms really at the surface on a few atomic layers if not one.

$$\mathbf{P}_{\text{Surface}}^{2\omega} = \chi^{(2)}(2\omega;\ \omega,\omega)\colon \mathbf{E}(\omega)\ \mathbf{E}(\omega) \tag{2.5}$$

where $\chi^{(2)}$ represents the second order nonlinear susceptibility and $\mathbf{E}(\omega)$ is the fundamental electric field with ω frequency. Secondly, the bulk contribution (quadrupole) comes from the crystalline nature of the material and does not exist for amorphous. Even if the crystalline material is centrosymmetric in the context of linear dipolar approximation, it can be proved that it is no more the case if we consider multipolar field expansion. It can be understood this effect as being due to an inhomogeneous field distribution at the scale of the crystal cell (Gielis et al., 2008). The bulk contribution can be described in Equation (2.6) and k_ω is the wave vector of the fundamental electric field in semiconductor (Gielis et al., 2008) and derived from the gradient operator.

$$\mathbf{P}_{\text{bulk}}^{2\omega} = \chi^{(2),\text{QP}}(2\omega;\ \omega,\omega)\colon \mathbf{E}(\omega)\ \text{i}k_\omega\mathbf{E}(\omega) \tag{2.6}$$

where $\chi^{(2),\text{QP}}$ is the second-order quadrupole susceptibility and originated by electric quadrupole and magnetic dipole contributions. Finally, when a static electric field is present at the interface such as Si/SiO_2, a fourth rank tensor $\chi^{(3)}$ generates to SHG signal. The field induced contribution is given by

$$\mathbf{P}_{\text{efish}}^{2\omega} = \chi^{(3)}(2\omega;\ \omega, \omega, 0)\colon \mathbf{E}(\omega)\ \mathbf{E}(\omega)\ \mathrm{E}_{\mathrm{dc}} \tag{2.7}$$

where $\chi^{(3)}$ is third order nonlinear susceptibility. Additionally, E_{dc} is the static electric field inside the sample and it is perpendicular to the surface. EFISH term is identically equal to the 'regular' surface dipole contribution (Gielis et al.,2008).

To utilize the potential of SHG as a characterization method, it is necessary to understand these three contributions. In the following sections of this chapter, theoretical background of surface SHG, EFISH and bulk SHG are discussed, respectively.

2.1. Surface Second Harmonic Generation

Second harmonic generation is a powerful tool for characterization of surfaces and interfaces (Bloembergen et al., 1968; Marka et al., 2000; Park, 2010). This is due to high sensitivity of SHG to the surface and interface properties of centrosymmetric media. As mentioned before, SHG is forbidden in the bulk of the centrosymmetric media because of the inversion symmetry inside. However, at the interface and surface regions, the inversion symmetry is broken between dissimilar media. As a consequence, the electric dipole terms arises from the interface/surface. In addition, a discontinuity in the normal component of the electric field can generate higher order multipole terms. These two effects constitute surface dipole polarization (Lüpke, 1999). Therefore, the SHG at surface is governed by the second order nonlinear susceptibility tensor $\chi^{(2)}$, through the relation

$$\mathbf{P}^{(2)}(2\omega) = \epsilon_0 \chi^{(2)}\ \mathbf{E}(\omega)\mathbf{E}(\omega) \tag{2.8}$$

This equation proves that the electric field with the frequency ω produces the radiation at twice the frequency; i.e. 2ω. In the next of this section, the second order nonlinear susceptibility is found for a centrosymmetric media. Then, the phenomenological model for surface SHG, which is developed by Sipe (Sipe, 1987) and Sipe and Mizrahi (Mizrahi and Sipe, 1988), is shown briefly.

2.1.1. Second Order Nonlinear Susceptibility in Silicon

Silicon is the most commonly used material in microelectronic industry because it has the diamond-cubic and also centrosymmetric crystal structure. Therefore, in the bulk silicon, the electric field and the polarization vectors should be invariant under the inversion symmetry. In other words, if the coordinate system changes from **r** to **-r**, because of the same manner of the electric field **E** should be $-\mathbf{E}$ and also the second order polarization **P** produces $-\mathbf{P}$. As mentioned before, the relationship for second order nonlinear polarization is $\mathbf{P}^{2\omega} = \epsilon_0 \chi^{(2)} \mathbf{E}(\omega)\mathbf{E}(\omega)$. Under the inversion symmetry in the material;

$$\begin{aligned} -\mathbf{P}^{2\omega} &= \epsilon_0 \chi^{(2)}(-\mathbf{E}(\omega))(-\mathbf{E}(\omega)) \\ &= \epsilon_0 \chi^{(2)} \mathbf{E}(\omega)\mathbf{E}(\omega) = \mathbf{P}^{(2)} \end{aligned} \tag{2.9}$$

In this case, $\mathbf{P}^{2\omega}$ can be equal $-\mathbf{P}^{2\omega}$ if $\chi^{(2)}$ vanish. So in the material, $\chi^{(2)}_{\text{bulk}} = 0$. However, the inversion symmetric material can generate SHG from higher order nonlinear responses such as magnetic dipole and electric quadrupole responses. In addition, at the surface, the inversion symmetry is broken along the direction of the surface normal. Thus $\chi^{(2)}_{\text{surface}} \neq 0$. This results in the electric dipole contribution. In Cartesian coordinates, the tensor relation between the amplitudes of the electric field **E** and the polarization **P** can be shown by

$$\mathrm{P}_{\mathrm{i}}^{2\omega} = \sum_{\mathrm{jk}} \chi^{(2)}_{\mathrm{ijk}} \mathrm{E}_{\mathrm{j}}(\omega)\mathrm{E}_{\mathrm{k}}(\omega) \tag{2.10}$$

Here the indices 'ijk' refer to laboratory coordinates as shown in Figure 2.1 Also $\mathrm{P}_{\mathrm{i}}^{2\omega}$ is the induced polarization at the second harmonic frequency, and $\mathrm{E}_{\mathrm{i}}(\omega)$ is the electric field at the fundamental frequency. They can be written:

$$\mathbf{P}^{(2)} = \begin{pmatrix} \mathrm{P}_{\mathrm{x}}^{(2)} \\ \mathrm{P}_{\mathrm{y}}^{(2)} \\ \mathrm{P}_{\mathrm{z}}^{(2)} \end{pmatrix} \text{ and } \mathbf{E} = \begin{pmatrix} \mathrm{E}_{\mathrm{x}} \\ \mathrm{E}_{\mathrm{y}} \\ \mathrm{E}_{\mathrm{z}} \end{pmatrix} \tag{2.11}$$

The second order nonlinear susceptibility tensor $\chi_{ijk}^{(2)}$ has 27 components and is shown as (Park, 2010):

$$\chi_{ijk}^{(2)} = \begin{pmatrix} \chi_{xxx} & \chi_{xxy} & \chi_{xxz} & \chi_{xyx} & \chi_{xyy} & \chi_{xyz} & \chi_{xzx} & \chi_{xzy} & \chi_{xzz} \\ \chi_{yxx} & \chi_{yxy} & \chi_{yxz} & \chi_{yyx} & \chi_{yyy} & \chi_{yyz} & \chi_{yzx} & \chi_{yzy} & \chi_{yzz} \\ \chi_{zxx} & \chi_{zxy} & \chi_{zxz} & \chi_{zyx} & \chi_{zyy} & \chi_{zyz} & \chi_{zzx} & \chi_{zzy} & \chi_{zzz} \end{pmatrix} \quad (2.12)$$

The second order susceptibility $\chi_{ijk}^{(2)}$ is symmetrical because SHG is not related to the orientation of the electric field which is oscillating at optical frequencies. Therefore, it has the same effect in the last two indices, $\chi_{ijk}^{(2)} = \chi_{ikj}^{(2)}$ (the other way is that $E_j E_k$ can replace $E_k E_j$). Due to these symmetries of the nonlinear susceptibility tensor, it can reduce to 18 independent components. The relationship between the polarization and the electric field can be written as the following

$$\begin{pmatrix} P_x^{(2)} \\ P_y^{(2)} \\ P_z^{(2)} \end{pmatrix} = \begin{pmatrix} \chi_{xxx} & \chi_{xyy} & \chi_{xzz} & \chi_{xyz} & \chi_{xxz} & \chi_{xxy} \\ \chi_{yxx} & \chi_{yyy} & \chi_{yzz} & \chi_{yyz} & \chi_{yxz} & \chi_{yxy} \\ \chi_{zxx} & \chi_{zyy} & \chi_{zzz} & \chi_{zyz} & \chi_{zxz} & \chi_{zxy} \end{pmatrix} . \begin{pmatrix} E_x E_x \\ E_y E_y \\ E_z E_z \\ 2. E_y E_z \\ 2. E_x E_z \\ 2. E_x E_y \end{pmatrix} \quad (2.13)$$

A significant point is that $\chi_{ijk}^{(2)}$ depends on the medium. Centrosymmetric materials have an inversion center symmetry. The only inversion symmetry is present in the $\hat{x} - \hat{y}$ plane while it is broken along the z direction in Figure 2.1.

For the (100) face, which has four-fold (C_{4v}) symmetry, the matrix in Equation (2.13) has only five nonzero components of the second order nonlinear susceptibility as mentioned by Sipe et al. in his early work (Sipe et al., 1987),

$$\begin{pmatrix} P_x^{(2)} \\ P_y^{(2)} \\ P_z^{(2)} \end{pmatrix} = \begin{pmatrix} 0 & 0 & 0 & 0 & \chi_{xxz} & 0 \\ 0 & 0 & 0 & \chi_{yyz} & 0 & 0 \\ \chi_{zxx} & \chi_{zyy} & \chi_{zzz} & 0 & 0 & 0 \end{pmatrix} . \begin{pmatrix} E_x E_x \\ E_y E_y \\ E_z E_z \\ 2. E_y E_z \\ 2. E_x E_z \\ 2. E_x E_y \end{pmatrix} \quad (2.14)$$

where χ_{zzz}, $\chi_{zxx} = \chi_{zyy}$ and $\chi_{yyz} = \chi_{xxz}$ are nonzero independent components (Gielis et al., 2008; Lüpke et al., 1994). $\hat{X}$- and $\hat{y}$-axis lie on the surface/interface and z-axis is normal to x and y plane as shown in Figure 2.1.

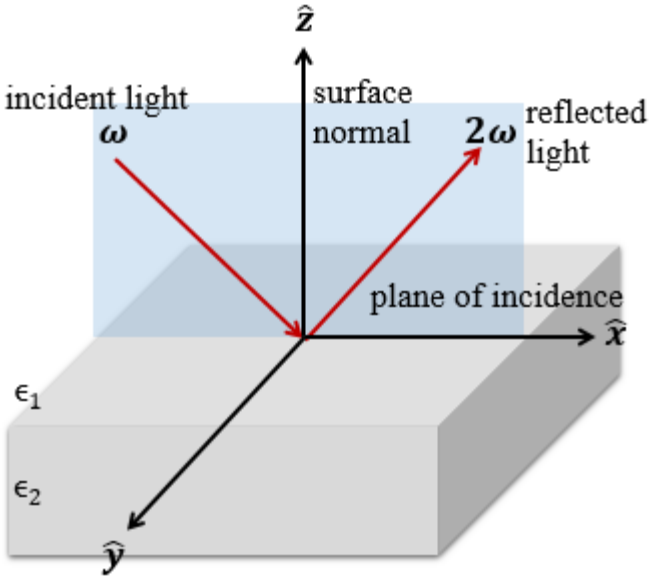

Figure 2.1. Schematic of the Cartesian coordinate system on surface SHG between two dissimilar mediums. Due to the inversion symmetry, SHG is forbidden in the bulk but can occur only at the surface.

2.1.2. Phenomenological Model of Time Independent Second Harmonic Generation from Surface/Interface

This section aims to describe the phenomenological model of surface second harmonic generation briefly. The model was developed by Sipe (Sipe, 1987) and Sipe and Mizrahi (Mizrahi & Sipe, 1988), which is originated the earlier work of Heinz (Heinz, 1982) and Bloembergen and Pershan (Bloembergen N., 1962). According to this phenomenological model, a thin dipole sheet (just above) at the interface is assumed a second harmonic source. Basically, like in Figure 2.1, the incident plane wave reflects with different frequencies from the interface between two different dielectric mediums such as air and silicon. The second frequency is generated by the dipole sheet which is described in section 2.1.2.3. Then using Green function formalism, Sipe (Sipe, 1987) calculated the S and P components of the electromagnetic field which are generated by the source. Afterwards, Mizrahi and Sipe (Mizrahi & Sipe, 1988) used Fresnel coefficients for four different experimental geometries which are obtained by Heinz

(Heinz, 1982). They found same expression of SHG intensity in all cases. In this section, we will consider just one geometry in Figure 2.1.

The outline of this section is in order; firstly, it starts with the Maxwell's equation as in the most of all physical problems. Then, the basic principles of Coordinate system are demonstrated to describe the vector fields of the electromagnetic wave. Later, the dipole sheet is defined and so the Maxwell's equation is discussed again to correspond to this dipole sheet. In addition, the components of the electric field are found in these conditions. Next, Fresnel coefficients are used to find the generated second harmonic fields in a specific geometry. Finally, the SHG intensity are calculated for different polarization states.

2.1.2.1. Maxwell's Equations in Homogenous Medium

Electromagnetic wave propagating can be summarized into the famous Maxwell's equations by four particular equations, which are related to five vectors **E** (the electric field), **D** (the electric displacement field), **H** (the magnetic field intensity), **B** (the magnetic field), **J** (the current density) and the scalar field $\boldsymbol{\rho}$ (the volume charge density). We are initially interested in the solutions of Maxwell's equation in the medium which there are no free electric charges or currents. It means that **J** and $\boldsymbol{\rho}$ are equal zero, so the macroscopic Maxwell's equations are given by

$$\boldsymbol{\nabla} \cdot \mathbf{D} = 0 \tag{2.15a}$$

$$c\boldsymbol{\nabla} \times \mathbf{H} - \dot{\mathbf{D}} = 0 \tag{2.15b}$$

$$\boldsymbol{\nabla} \cdot \mathbf{B} = 0 \tag{2.15c}$$

$$c\boldsymbol{\nabla} \times \mathbf{E} + \dot{\mathbf{B}} = 0 \tag{2.15d}$$

The displacement and magnetizing field **D**, **H** are related to the electric and magnetic field. It is called the *Constitutive relations*. In Gaussian units, they are described by

$$\mathbf{D} = \mathbf{E} + 4\pi\mathbf{P_t} \tag{2.16a}$$

$$\mathbf{H} = \mathbf{B} - 4\pi\mathbf{M_t} \tag{2.16b}$$

The vectors $\mathbf{P_t}$ and $\mathbf{M_t}$ represent the total electric and magnetic dipole moments per unit volume of a medium respectively. These quantities give information about the electric and magnetic field in the medium.

$$\mathbf{P_t} = \chi_e^{(1)}\mathbf{E} + \mathbf{P} \tag{2.17a}$$

$$\mathbf{M_t} = \chi_b^{(1)}\mathbf{B} + \mathbf{M} \tag{2.17b}$$

Here the susceptibilities χ_e and χ_b are known as the linear response of the medium at the frequency ω. Also, the **P** is the polarization and **M** is the magnetization of the optical medium. The difference between $\mathbf{P_t}$ and **P** or $\mathbf{M_t}$ and **M** is that the total electric and magnetic dipole moments are nonlocal functions, whereas the polarization and magnetization are local functions (Shen, 2002). The polarization **P** and **M** are the only parameters which gives information about how optical medium is affected by light. In nonlinear optics, they are complicated nonlinear functions of **E** and **B**. However, when the **E** and **B** are relatively small, the polarization **P** and the magnetization **M** depends on the linear functions of **E** and **B**. Initially **P** and **M** are assumed that they are equal to zero (Sipe, 1987). Therefore, **D** and **H** take these forms;

$$\begin{aligned}\mathbf{D} &= \mathbf{E} + 4\pi\mathbf{P_t} \\ &= \mathbf{E} + 4\pi\left(\chi_e^{(1)}\mathbf{E}\right) \\ &= \left(1 + 4\pi\,\chi_e^{(1)}\right) = \epsilon\,\mathbf{E}\end{aligned} \tag{2.18a}$$

$$\begin{aligned}\mathbf{H} &= \mathbf{B} - 4\pi\mathbf{M_t} \\ &= \mathbf{B} - 4\pi(\chi_b^{(1)}\mathbf{B}) \\ &= \left(1 - 4\pi\,\chi_b^{(1)}\right) = \mu^{-1}\mathbf{B}\end{aligned} \tag{2.18b}$$

where the linear constant $\epsilon = 1 + 4\pi\,\chi_e^{(1)}$ is the permittivity of the material and the linear constant $\mu^{-1} = 1 - 4\pi\,\chi_b^{(1)}$ is the permeability of the material. It is studied the stationary continuous waves; it means that all the vector fields are constant with respect to time. In homogenous media, the solution of Maxwell's equations is calculated as (see detail in Appendix A)

$$\nabla \cdot \mathbf{E}(\mathbf{r}) = 0 \tag{2.19a}$$

$$\nabla \times \mathbf{B}(\mathbf{r}) + i\tilde{\omega}\epsilon\mu\mathbf{E}(\mathbf{r}) = 0 \tag{2.19b}$$

$$\nabla \cdot \mathbf{B}(\mathbf{r}) = 0 \tag{2.19c}$$

$$\nabla \times \mathbf{E}(\mathbf{r}) - i\tilde{\omega}\mathbf{B}(\mathbf{r}) = 0 \tag{2.19d}$$

where $\tilde{\omega} = \omega/c$. These equations can be used to find the components of electromagnetic fields in any homogeneous medium.

2.1.2.2. Basic Principles

In most SHG experiments for surfaces and interfaces, the incident monochromatic beam of frequency ω on the substrate at an angle θ_i can generate SHG light in reflection or transmission. In Figure 2.2, the wave vectors $\boldsymbol{\nu_0}$, $\boldsymbol{\nu}_+$ and $\boldsymbol{\nu}_-$ represent the incident, reflected and transmitted fundamental lights respectively. They can be expressed as upward for ν_+ and downward for ν_- propagating evanescent wave due to the change in the z direction (Sipe, 1987). They are demonstrated by

$$\begin{aligned} \boldsymbol{\nu}_+ &= u\hat{x} + v\hat{y} + w\hat{z} = \kappa\hat{\kappa} + w\hat{z} \\ \boldsymbol{\nu}_- &= u\hat{x} + v\hat{y} - w\hat{z} = \kappa\hat{\kappa} - w\hat{z} \end{aligned} \tag{2.20}$$

Here, Sipe (Sipe, 1987) uses another vector $\boldsymbol{\kappa} = u\hat{x} + v\hat{y}$ but examines special case which is $\hat{\kappa} = \hat{x}$.

For simplicity, p-polarization (E-field is parallel to the plane of incidence, along $\hat{x} - \hat{z}$ plane) and s-polarization (E-field is orthogonal to the plane of incidence, along $\hat{y}$) states are considered for the fundamental and harmonic lights. According to the Figure 2.2, it can be easily seen that the relationship between the unit vectors; $\hat{s}$, $\hat{p}$ and $\hat{v}$ are in these form (Sipe, 1987);

$$\hat{s} \times \hat{v}_\pm = \hat{p}_\pm , \qquad \hat{v}_\pm \times \hat{p}_\pm = \hat{s}, \qquad \hat{p}_\pm \times \hat{s} = \hat{v}_\pm \tag{2.21}$$

where $\hat{p}_\pm = \nu^{-1}(\kappa\hat{z} \mp w\hat{\kappa})$. The electromagnetic waves **E** and **B** have s- and p-polarization components, and propagate in upward and downward directions.

Immediately, the upward propagating electric field $\mathbf{E}_+$ and the downward propagating electric field $\mathbf{E}_-$ can be determined as

$$\mathbf{E}_+(\mathbf{r}) = (E_{s+}\hat{s} + E_{p+}\hat{p}_+)\exp(i\nu_+ \cdot \mathbf{r}) \tag{2.22a}$$

$$\mathbf{E}_-(\mathbf{r}) = (E_{s-}\hat{s} + E_{p-}\hat{p}_-)\exp(i\nu_- \cdot \mathbf{r}) \tag{2.22b}$$

In addition, the magnetic field expressions for upward and downward propagating wave are found by using fourth equation of the macroscopic Maxwell's equations (in Equation (2.19d)).

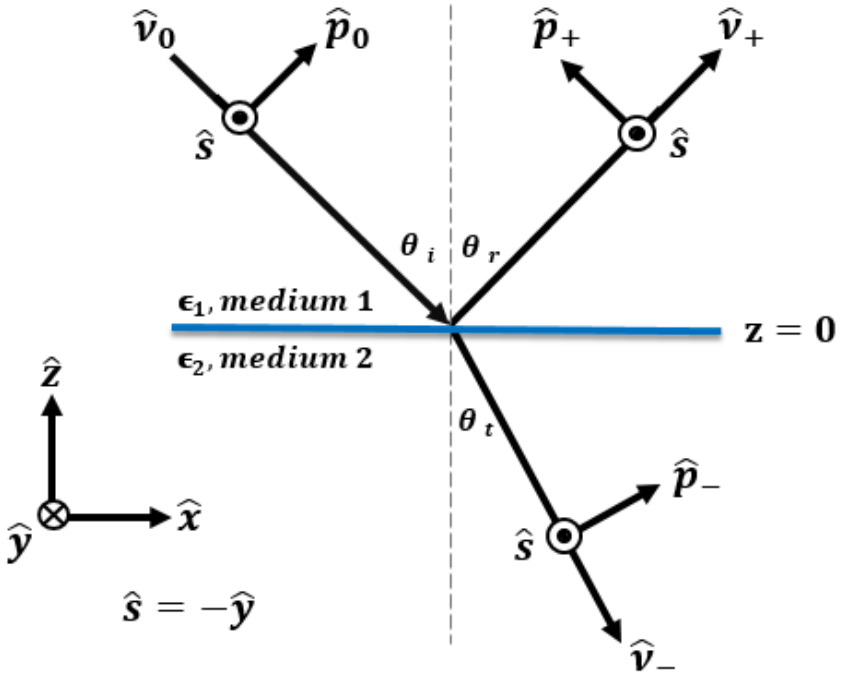

Figure 2.2. Geometry of the incident, reflected and transmitted wave vectors at the surface ($z = 0$) between two different dielectric mediums (ϵ_1, ϵ_2) in Cartesian coordinate.

They are shown as

$$\mathbf{B}_+(\mathbf{r}) = \sqrt{\mu\epsilon}(E_{p+}\hat{s} - E_{s+}\hat{p}_+)\exp(i\nu_+ \cdot \mathbf{r}) \tag{2.23a}$$

$$\mathbf{B}_-(\mathbf{r}) = \sqrt{\mu\epsilon}(E_{p-}\hat{s} - E_{s-}\hat{p}_-)\exp(i\nu_- \cdot \mathbf{r}) \tag{2.23b}$$

Here $\sqrt{\mu\epsilon}$ represents the refractive index of the medium, called as n. The aim for describing the electromagnetic field is to find the components of the fields and afterwards to evaluate the intensity of SH light.

2.1.2.3. Inhomogeneous Maxwell's Equations and Dipole Sheet

The phenomenological model for treating SHG from surfaces and interfaces, which was developed by Sipe (Sipe, 1987) and then Sipe and Mizrahi (Mizrahi & Sipe, 1988), uses a thin dipole sheet sitting at $z_o = 0^+$ as a second harmonic source as shown in Figure 2.3. Due to this dipole sheet, the homogenous Maxwell's equations cannot be used because the polarization $\mathbf{P}(\mathbf{r})$ cannot be zero anymore (like in Equation 2.18a). Therefore, the homogeneous Maxwell's equations turn into inhomogeneous form (Sipe, 1987) by taking $\mathbf{P}(\mathbf{r}) \neq 0$ (we consider just for non-magnetic material, so still $\mathbf{M}(\mathbf{r}) = 0$) (see the calculation detail to Appendix B):

$$\boldsymbol{\nabla} \cdot \mathbf{E}(\mathbf{r}) = -4\pi\epsilon^{-1}\boldsymbol{\nabla} \cdot \mathbf{P}(\mathbf{r}) \tag{2.24a}$$

$$\boldsymbol{\nabla} \times \mathbf{B}(\mathbf{r}) + i\tilde{\omega}\epsilon\mu\mathbf{E}(\mathbf{r}) = -4\pi i\tilde{\omega}\mu\mathbf{P}(\mathbf{r}) \tag{2.24b}$$

$$\boldsymbol{\nabla} \cdot \mathbf{B}(\mathbf{r}) = 0 \tag{2.24c}$$

$$\boldsymbol{\nabla} \times \mathbf{E}(\mathbf{r}) - i\tilde{\omega}\mathbf{B}(\mathbf{r}) = 0 \tag{2.24d}$$

Now, these inhomogeneous Maxwell's equations can be used to find the components of the electromagnetic fields. However, the source $\mathbf{P}(\mathbf{r})$ and the total electric field $\mathbf{E}(\mathbf{r})$ and magnetic field $\mathbf{B}(\mathbf{r})$ need to be described under these conditions. First, to model the electromagnetic properties at the interface, the polarization sheet, oscillating at frequency ω, $\mathbf{P}(\mathbf{r})$ can be expressed as

$$\mathbf{P}(\mathbf{r}) = P\,\delta(z - z_o)\exp(i\boldsymbol{\kappa} \cdot \mathbf{R}) \tag{2.25}$$

It has a plane wave behavior with a spatial variation indicated by a wave vector $\boldsymbol{\kappa}$ (parallel to the surface) and $\mathbf{R} = (x, y)$ in Figure 2.3. Here, the Dirac delta δ represents that the

dipole sheet can exist just at one point $z_o = 0^+$that is approximately an atomic distance above the interface.

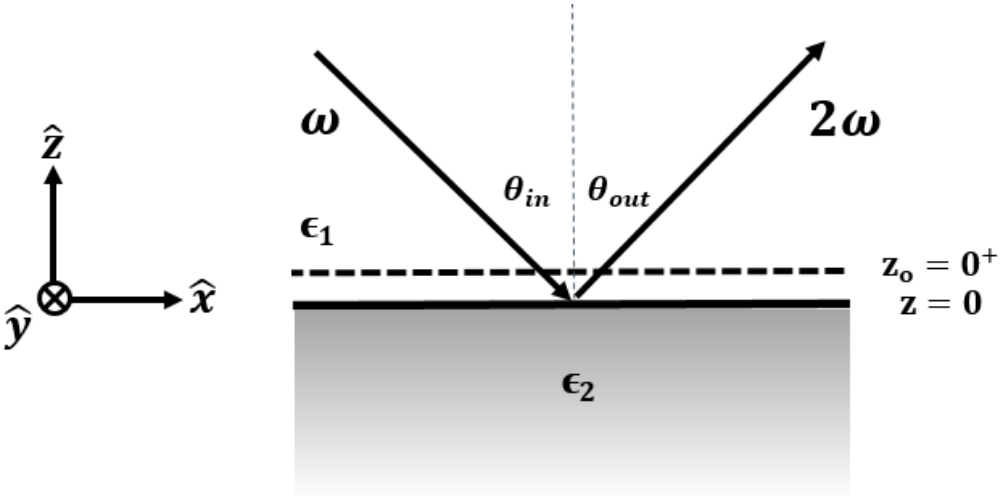

Figure 2.3. Illustration of the dipole sheet (at $z_o = 0^+$) on the surface

In addition, this dipole sheet can produce also an additional vector field $\boldsymbol{\xi}$ to the total electric field at $z_{o+} = 0^+$. It can be demonstrated by

$$\boldsymbol{\xi} = \xi_s \hat{\boldsymbol{s}} + \xi_\kappa \hat{\boldsymbol{\kappa}} + \xi_z \hat{\boldsymbol{z}} \tag{2.26}$$

Finally, the total electric and magnetic fields can be described as:

$$\mathbf{E}(\mathbf{r}) = \mathbf{E}_+(\mathbf{r}) \exp(-i\omega z_o)\, h(z - z_o) + \mathbf{E}_-(\mathbf{r}) \exp(i\omega z_o)\, h(z_o - z) \tag{2.27a}$$

$$+\boldsymbol{\xi}\delta(z - z_o) \exp(i\kappa \cdot \boldsymbol{R})$$

$$\mathbf{B}(\mathbf{r}) = \mathbf{B}_+(\mathbf{r}) \exp(-i\omega z_o)\, h(z - z_o) + \mathbf{B}_-(\mathbf{r}) \exp(i\omega z_o)\, h(z_o - z) \tag{2.27b}$$

where $h(z)$ is the step function to represent the directions of the propagating wave, and generally it can be identified as $h(z) = 1$ when $z > 0$ and $h(z) = 0$ when $z < 0$. Therefore, $h(z - z_o)$ is for the upward wave ones and $h(z_o - z)$ is for the downward wave ones. After putting Equations (2.27) into Equation (2.24b) and Equation (2.24d), we can find (see Appendix C) $\xi_s = \xi_\kappa = 0$ and $\xi_z = -4\pi\epsilon^{-1}P_z$. The components of the electric field are found in these forms

$$E_{s\pm} = \frac{2\pi i\tilde{\omega}^2}{w}\hat{s}\cdot P \tag{2.28a}$$

$$E_{p\pm} = \frac{2\pi i\tilde{\omega}^2}{w}\hat{p}_{\pm}\cdot P \tag{2.28b}$$

These two s and p components of the waves are at frequency ω. These components will help us to find to generated second harmonic light and the SHG intensity.

2.1.2.4. Generated Fields and Second Harmonic Generation Intensity

In this section, the intensity of second harmonic light is specified according to the second-order nonlinear susceptibility. So far, the s- and p-polarization electric field components in both upward and downward directions have been found at frequency ω. Furthermore, the polarization sheet is taken at oscillating 2ω is sitting at $\mathrm{z} = 0^{+}$

$$\mathbf{P^{2\omega}}(\mathbf{r}) = P^{2\omega}(\mathbf{R})\,\delta(\mathrm{z}-0^{+})\exp(2i\boldsymbol{\kappa}\cdot\mathbf{R}) \tag{2.29}$$

The polarization of SHG is originated by second-order nonlinear susceptibility tensor which is defined with the respect to the electric field at $\mathrm{z} = 0^{-}$ (Mizrahi V., 1988; Lüpke, 1999). Therefore,

$$P^{2\omega}(\mathbf{R}) = \chi^{(2)}\colon \mathbf{E}^{\omega}(\mathbf{R},\mathrm{z}=0^{-})\mathbf{E}^{\omega}(\mathbf{R},\mathrm{z}=0^{-}) \tag{2.30}$$

where the electric field $\mathbf{E}^{\omega}$ induce the dipole sheet at frequency ω. Because of the definition of the second-order nonlinear susceptibility tensor at $\mathrm{z} = 0^{-}$, $\mathbf{E}^{\omega}$ should be the transmitted fundamental light into the medium ϵ_2. First we define that the fundamental light as shown in Figure 2.4 (Mizrahi & Sipe, 1988). It has s- and p_{0-} polarization components which indicate the incident downward-propagating wave:

$$\begin{aligned}\mathbf{E_{in}^{\omega}}(\mathbf{r}) &= (E_{in}^{s}\hat{s} + E_{in}^{p}\hat{p}_{0-})\exp[i(\kappa x - w_o z)]\\ &= \left(\frac{E_{in}^{s}}{|E_{in}|}\hat{s} + \frac{E_{in}^{p}}{|E_{in}|}\hat{p}_{0-}\right)|E_{in}|\exp[i(\kappa x - w_o z)]\\ &= \hat{e}^{\,in}|E_{in}|\exp[i(\kappa x - w_o z)]\end{aligned} \tag{2.31}$$

where $|E_{in}|^2 = |E_{in}^s|^2 + |E_{in}^p|^2$. However, to define transmitted fundamental light and generated second harmonic light, we need to use the Fresnel coefficients. They are defined in Table 2.1.

Table 2.1. Definitions of the symbol of the Fresnel coefficients

$\boldsymbol{\omega}$	$\boldsymbol{2\omega}$	**Definition**
$r_{ij}^{s,p}$	$R_{ij}^{s,p}$	Reflection coefficient from medium i to j
$t_{ij}^{s,p}$	$T_{ij}^{s,p}$	Transmission coefficient from medium i to j

Therefore, the fundamental transmitted light into the medium 2 can be written as

$$\begin{aligned}\mathbf{E_t^{\omega}}(\mathbf{r}) &= (E_{in}^s t_{12}^s \hat{s} + E_{in}^p t_{12}^p \hat{p}_-)\exp[i(\kappa x - wz)] \\ &= \left(\frac{E_{in}^s}{|E_{in}|} t_{12}^s \hat{s} + \frac{E_{in}^p}{|E_{in}|} t_{12}^p \hat{p}_-\right)|E_{in}|\exp[i(\kappa x - wz)] \\ &= \mathbf{e^{\omega}}|E_{in}|\exp(i\kappa x) \qquad (2.32)\end{aligned}$$

Now, we can put $\mathbf{E_t^{\omega}}(\mathbf{r})$ into the induced nonlinear polarization $P^{2\omega}(\mathbf{R})$ and can be found

$$P^{2\omega}(\mathbf{R}) = \chi^{(2)}\mathbf{:}\, \mathbf{e^{\omega}e^{\omega}}|E_{in}|^2 \qquad (2.33)$$

There are two possibilities to generate second harmonic light as shown in Figure 2.4. After the incident light induces to the dipole sheet, it creates an upward and downward propagating waves at frequency 2ω. Therefore, the first one is that the directly generated upward wave. The second one is that a part of the downward SHG wave can reflect upward at z=0 (Mizrahi & Sipe, 1988). It is illustrated in Figure 2.4. We use uppercase symbols for second harmonic light, such as $\hat{P}_{0\mp}$ indicates the upward or downward p-polarized propagating wave at frequency 2ω in the first medium with the dielectric constant ϵ_1. However, the symbol of $\hat{p}_{0-}$ is for the fundamental downward propagating wave in the same medium and $\hat{p}_-$ in the second medium ϵ_2.

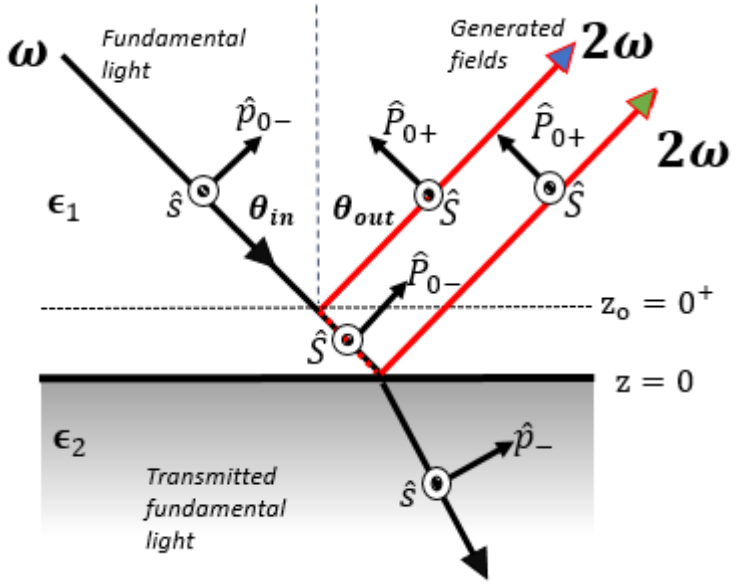

Figure 2.4. Illustration of the fundamental light; the transmitted fundamental and the generated second harmonic lights at the interface between two different mediums 1 and 2 with dielectric constants ϵ_1 and ϵ_2. The black colored lines represent the fundamental lights at ω wavelenght. The red colored lines are for generated second harmonic light at 2ω wavelength. The one with the blue arrow is directly generated upward-propagating wave, and the other one with the green arrow is generated downward-propagating wave which reflect at $z = 0$ towards to upward.

Finally, the generated second harmonic light can be written in this form:

$$\mathbf{E^{2\omega}}(\mathbf{r}) = \left(E_{in}^{s}\hat{S} + E_{in}^{p}\hat{P}_{0+}\right) exp[i(2\kappa x + W_0 z)] + \left(E_{in}^{s}R_{12}^{s}\hat{S} + E_{in}^{p}R_{12}^{p}\hat{P}_{0-}\right) exp[i(2\kappa x + W_0 z)] \quad (2.34)$$

The first and second term of Equation (2.34) represent generated upward-propagating and reflected downward-propagating second harmonic wave by the dipole sheet, respectively. For the second term, we use the reflection Fresnel coefficient from medium 1 to 2, as called $R_{12}^{s,p}$. Here, we consider $\theta_{in} = \theta_{out}$. Then, Equation (2.34) takes this form:

$$\begin{aligned}\mathbf{E^{2\omega}}(\mathbf{r}) &= \left[E_{in}^{s}(1 + R_{12}^{s})\,\hat{S} + E_{in}^{p}\left(\hat{P}_{0+} + R_{12}^{p}\hat{P}_{0-}\right)\right] \exp[i(2\kappa x + W_0 z)] \\ &= \left[\frac{E_{in}^{s}}{|E_{in}|}(1 + R_{12}^{s})\,\hat{S} + \frac{E_{in}^{p}}{|E_{in}|}\left(\hat{P}_{0+} + R_{12}^{p}\hat{P}_{0-}\right)\right] |E_{in}| \exp[i(2\kappa x + W_0 z)] \\ &= \mathbf{e}^{2\omega}|E_{in}| \exp[i(2\kappa x + W_0 z)]\end{aligned} \quad (2.35)$$

where $\mathbf{e}^{2\omega} = \left[\frac{E_{in}^{s}}{|E_{in}|}(1 + R_{12}^{s})\,\hat{S} + \frac{E_{in}^{p}}{|E_{in}|}\left(\hat{P}_{0+} + R_{12}^{p}\hat{P}_{0-}\right)\right]$. The intensity of second harmonic light is proportional to the square root of the second harmonic light electric field; $\mathbf{I}(2\omega) = \left|\mathbf{E^{2\omega}}(\mathbf{r})\right|^{\mathbf{2}}$. So, it is calculated

$$\left|\mathbf{E^{2\omega}}\right|^{2} = |\mathbf{e}^{2\omega}|^{2}|E_{in}|^{2} \tag{2.36}$$

where $|E_{in}|^{2} = |E_{in}^{s}|^{2} + \left|E_{in}^{p}\right|^{2}$. To denote the s- and p- polarized second harmonic light, which are generated by the dipole sheet, we use Capital letters for polarization states such as $\hat{S}$ and $\hat{P}_{\pm}$. They can be written by

$$E_{s\pm} = \frac{2\pi i\widetilde{\Omega}^{2}}{W_{0}}\hat{S}\cdot P^{2\omega}(\mathbf{R}) \tag{2.37a}$$

$$E_{p\pm} = \frac{2\pi i\widetilde{\Omega}^{2}}{W_{0}}\hat{P}_{\pm}\cdot P^{2\omega}(\mathbf{R}) \tag{2.37b}$$

where $\Omega = 2\omega$ and $P^{2\omega}(\mathbf{R}) = \chi^{(2)}\!:\mathbf{e^{\omega}e^{\omega}}|E_{in}|^{2}$. Putting the s- and p-polarization components of second harmonic electric field, finally we can get

$$\left|\mathbf{E^{2\omega}}\right|^{2} = \frac{4\pi^{2}\widetilde{\Omega}^{4}}{{W_{0}}^{2}}\left|\mathbf{e}^{2\omega}\cdot\chi^{(2)}\!:\mathbf{e^{\omega}e^{\omega}}\right|^{2}|E_{in}|^{4} \tag{2.38}$$

Here $\widetilde{\Omega}^{2}/\,{W_{0}}^{2} = \sec^{2}\theta_{in}$. After putting $\widetilde{\Omega}^{2} = 4\omega^{2}/c$ into and multiplying both sides of the equation by $(c/2\omega)^{2}$, the Equation (2.38) turns into

$$\frac{c}{2\pi}\left|\mathbf{E^{2\omega}}\right|^{2} = \frac{32\pi^{3}\omega^{2}}{c^{3}}\sec^{2}\theta_{in}\left|\mathbf{e}^{2\omega}\cdot\chi^{(2)}\!:\mathbf{e^{\omega}e^{\omega}}\right|^{2}\left(\frac{c}{2\pi}|E_{in}|^{2}\right)^{2} \tag{2.39}$$

Therefore, the intensity of second harmonic light;

$$I^{2\omega} = \frac{32\pi^{3}\omega^{2}}{c^{3}}\sec^{2}\theta_{in}\left|\mathbf{e}^{2\omega}\cdot\chi^{(2)}\!:\mathbf{e^{\omega}e^{\omega}}\right|^{2}(I^{\omega})^{2} \tag{2.40}$$

In Equation (2.40), the SHG intensity is proportional to the fundamental light intensity, I^{ω}. Now, this equation can be used to find the S- and P-polarized SHG intensity.

2.1.2.5. P- and S- Polarized Second Harmonic Generation Intensity

In this section, the intensity of S- and P-polarized SH light are calculated in terms of different polarized states of the fundamental light. The incident and reflected light are indicated as in Figure 2.5. The pumping light with the angle of incidence $\theta_1(\omega)$ is reflected from the surface or interface with a reflection angle of $\theta_1(2\omega)$. In addition, the refraction light in medium has two angle related to their frequency $\theta_2(\omega)$ and $\theta_2(2\omega)$ which are described

$$\theta_2(\varphi) = \sin^{-1}\left(\frac{\sqrt{\varepsilon_1(\varphi)}}{\sqrt{\varepsilon_2(\varphi)}}\sin\theta_1(\varphi)\right) \qquad \varphi = \omega, 2\omega \tag{2.41}$$

The intensity of SH light depends on the selected polarizer angle of the incident (input) light and the second harmonic (output) light. More precisely the polarization angle is the angle between the orientation of the electromagnetic electric field and the plane of incidence. In Figure 2.5, the symbols of γ_{in} and γ_{out} denote input and output polarization angles, respectively.

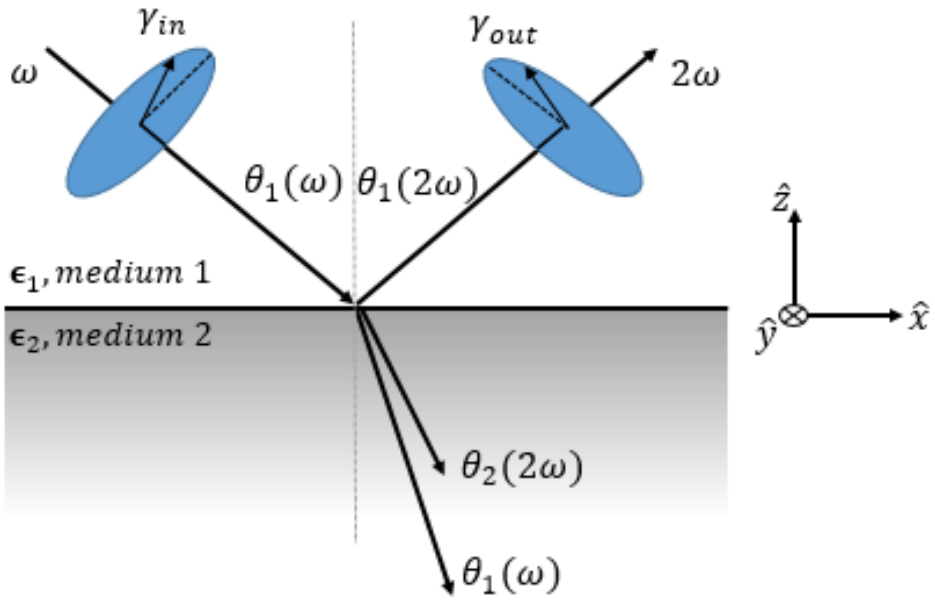

Figure 2. 5. Second harmonic generation optical geometry

As a result, $\gamma_{\text{in}} = 0$ corresponds to a rectilinearly P-polarized (TM) incident laser beam while $\gamma_{\text{in}} = 90°$ corresponds to a S-polarized (TE) incident one. Similarly, $\gamma_{\text{out}} =$

0 (resp. 90°) corresponds to a P (TM) (resp. (TE)) -polarized SH light. Experimentally both γ_{in} and γ_{out} can be varied continuously. In Equations (2.42), the S- polarized and the P- polarized SHG intensities are expressed (Kajikawa, Takezoe, & Fukuda, 1991) as functions of the polarization angle of incident light γ_{in}. They are described respectively

$$I_{sh}^{s}(\gamma_{in}) = K\,|E \sin\gamma_{in}\ \cos\gamma_{in}\ \chi_{izi}|^2 \tag{2.42a}$$

$$I_{sh}^{p}(\gamma_{in}) = K\left|A\cos^2_{\gamma_{in}}\chi_{zzz} - B\cos^2_{\gamma_{in}}\chi_{izi} + \left\{C\cos^2_{\gamma_{in}} + D\sin^2_{\gamma_{in}}\right\}\chi_{zii}\right|^2 \tag{2.42b}$$

A, B, C, D and E the coefficients which are determined from Fresnel equations and K coefficient is proportional to the intensity of the incident light. They are given in Table 2.2.

Table 2.2. The coefficients for Equation (2.42a) and Equation (2.42b) from one of the article of Kajikawa et al. (Source: Kajikawa et al., 1991)

Symbol	Coefficient
A	$8\frac{\varepsilon_{1(\omega)}\sqrt{\varepsilon_1(2\omega)}}{\varepsilon_2(\omega)\sqrt{\varepsilon_2(2\omega)}}\frac{cos^2\theta_1(\omega)sin^2\theta_1(\omega)sin^2\theta_2(\omega)sin^2\theta_1(2\omega)sin\theta_2(2\omega)}{cos^2(\theta_1(\omega)-\theta_2(\omega))\cos(\theta_1(2\omega)-\theta_2(2\omega))sin^2(\theta_1(\omega)+\theta_2(\omega))\sin(\theta_1(2\omega)+\theta_2(2\omega))}$
B	$16\frac{\sqrt{\varepsilon_1(\omega)}}{\sqrt{\varepsilon_2(\omega)}}\frac{cos^2\theta_1(\omega)\cos\theta_2(\omega)\cos\theta_1(2\omega)\cos\theta_2(2\omega)\sin\theta_1(\omega)sin^2\theta_2(\omega)\sin\theta_2(2\omega)}{cos^2(\theta_1(\omega)-\theta_2(\omega))\cos(\theta_1(2\omega)-\theta_2(2\omega))sin^2(\theta_1(\omega)+\theta_2(\omega))\sin(\theta_1(2\omega)+\theta_2(2\omega))}$
C	$8\frac{\sqrt{\varepsilon_1(2\omega)}}{\sqrt{\varepsilon_2(2\omega)}}\frac{cos^2\theta_1(\omega)cos^2\theta_2(\omega)sin^2\theta_2(\omega)sin^2\theta_1(2\omega)sin\theta_2(2\omega)}{cos^2(\theta_1(\omega)-\theta_2(\omega))\cos(\theta_1(2\omega)-\theta_2(2\omega))sin^2(\theta_1(\omega)+\theta_2(\omega))\sin(\theta_1(2\omega)+\theta_2(2\omega))}$
D	$8\frac{\sqrt{\varepsilon_1(2\omega)}}{\sqrt{\varepsilon_2(2\omega)}}\frac{cos^2\theta_1(\omega)sin^2\theta_2(\omega)sin^2\theta_1(2\omega)sin\theta_2(2\omega)}{\cos(\theta_1(2\omega)-\theta_2(2\omega))sin^2(\theta_1(\omega)+\theta_2(\omega))\sin(\theta_1(2\omega)+\theta_2(2\omega))}$
E	$16\frac{\sqrt{\varepsilon_1(\omega)}}{\sqrt{\varepsilon_2(\omega)}}\frac{cos^2\theta_1(\omega)cos\theta_1(2\omega)sin\theta_1(\omega)sin^2\theta_2(\omega)sin\theta_2(2\omega)}{\cos(\theta_1(\omega)-\theta_2(\omega))sin^2(\theta_1(\omega)+\theta_2(\omega))\sin(\theta_1(2\omega)+\theta_2(2\omega))}$
K	$\frac{32\,\pi^3\omega^2sec^2\theta_1(2\omega)}{c^3\varepsilon_1(\omega)\sqrt{\varepsilon_1(2\omega)}}I_0^2$

2.2. Electrical Field Induced Second Harmonic (EFISH)

In addition to surface contribution, there is another source effects to the SHG signal, in the case of the presence of a dc electric field close to the Si/ SiO_2 interface. It is called as EFISH (electric field induced second harmonic) and it was first discovered by Bloembergen and co-workers in 1967 (Lee et al., 1967). In their experiment, they observed SHG signal when they applied a dc electric field at the normal of silicon and silver surfaces. However, this discovery remained practically unnoticed for a number of years. Then, in 1981, Shen and co-workers resumed the interest to this effect in their work of surface-enhanced SHG (Chen et al., 1981). After a short time, surface-enhanced EFISH phenomenon was observed first time at a silver-electrolyte interface (Aktsipetrov et al., 1983). Nowadays, EFISH is mostly studied for investigation of the interface properties of the semiconductor-oxide materials (Damianos et al., 2016; Alles et al., 2007; Ionica et al., 2015). Because the interface between the silicon and its oxide is a very important studied field due to semiconductor device's importance in electronic device.

Some of the previous research has been done by H. M. van Driel et al. They observed the temporal behavior on SHG intensity (Bloch et al., 1995). Their results of time-dependent SHG intensity for Si(100) native oxide are shown in Figure 2.6. They used two different incident radiance of 3 kW cm^{-2} in Figure 2.6 (a) and 10 kW cm^{-2} in Figure 2.6 (b). They observed that the SHG signal arises in time and then saturates for both cases. However, at the lower radiance, the SHG light saturates a longer rise time than the other. Also, they explained that the silicon oxide (SiO_2) does not absorb wavelength at ω because of the larger band gap of the oxide (approximately 8.8 eV) (Bloch et al., 1995).

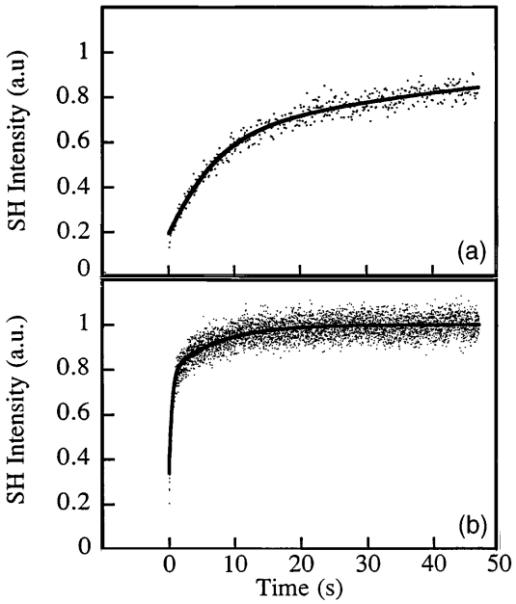

Figure 2.6. Time dependent SHG signal from Si(100) native oxide for (a) 3kW cm^{-2} and (b) 10 kW cm^{-2} (Source: Bloch et al., 1995)

As in Ref. (Gielis, Gevers et al., 2008) (Park et al.,2011; Bloch et al., 1996; Jun et al., 2004; Damianos et al., 2016) the time dependent electric field induced SHG from Si/SiO_2 interface is a third order process and it can be described in general by

$$I^{2\omega}(t) \propto \left|\chi^{(2)} + \chi^{(3)}E_{dc}(t)\right|^2 . (I^{\omega})^2 \tag{2.43}$$

where $\chi^{(2)}$ and $\chi^{(3)}$ are nonlinear second and third order tensors. $E_{dc}(t)$ is a quasi-static electric field across at the interface of Si/SiO_2 and it arises from the charge separation. The dc electric filed also exists near the interface of Si/SiO_2 without any applied external voltage. The electrons and holes in matter can be excited three and four photon absorption. It results in charge separation. The band offset between the silicon valence band and oxide conduction band is 4.5 eV (Park, 2010; Wang et al., 1998). The incoming light with the wavelength of 800nm corresponds to photon energy of 1.55 eV ($E=hc/\lambda$). The photons interact only with the silicon (its band gap is 1.1 eV) because their intensity is not enough to cross the band gap of the oxide which is 9 eV. Therefore, the electrons in the silicon valence band gain enough energy to pass the oxide surface by the three photon absorption after the photons interacts with the silicon surface. When the incoming light has enough energy for attracting the electrons at the valence band of the silicon, the electrons leave a hole state in silicon valence band and they travel to oxide surface. Then, the oxygen molecules in oxide surface capture the electrons which come from the silicon

surface. A Dc electric field occurs because of the charge separation between the remaining holes in the silicon valence band and the electrons captured by the oxygen molecules. This form is like capacitor structure. Additionally, the holes in the oxide can be also injected to the silicon. It means that the electrons in oxide can transfer to the silicon. Then it creates the holes in oxide. This is happened by four photon absorption. It induces opposite dc electric field at interface according to the electron injection in oxide. The probability of the four photon absorption is lower than the three photon absorption (Park, 2010). The schematic form of the electron and hole injection is illustrated in Figure 2.7 [(Park, 2010) (Figure 2.7)].

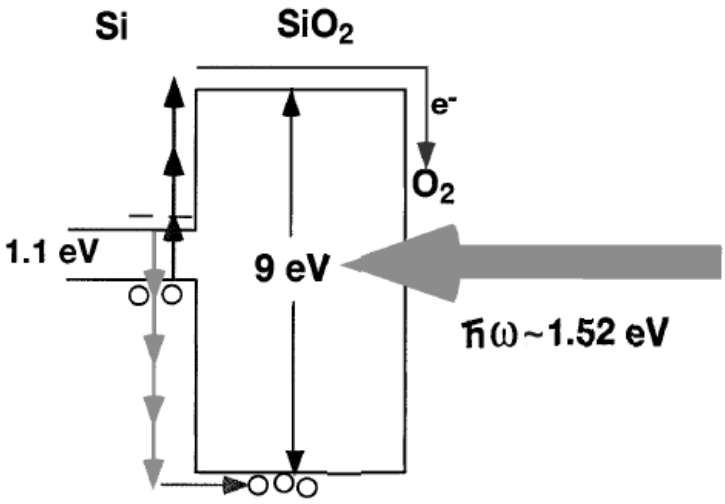

Figure 2.7. The illustration of the electron and hole injection on silicon system (Source: Park, 2010)

There are some dependencies which affects the saturated SHG level such as oxide thickness (Bloch, 1995), photon energy (Bloch et al., 1995; Wang et al., 1998), oxidation types (Ionica et al., 2015) and applied electric field (Jun et al., 2004). H. M. van Driel et al (Bloch et al., 1996) showed that time dependency behavior isn't observed if the thickness of oxide is thicker than 10 nm in Figure 2.8 (a). Additionally, W. Wang et al. (Wang et al., 1998) used different incidence photon energies. Their results demonstrated that increasing photon energy lead to decrease to saturated SHG signal level in Figure 2.8 (b). B. Jun et al showed that the SHG signal also strongly depends on the applied electric field and it can vary due to the charge trapping (Jun et al., 2004; Alles et al., 2007).

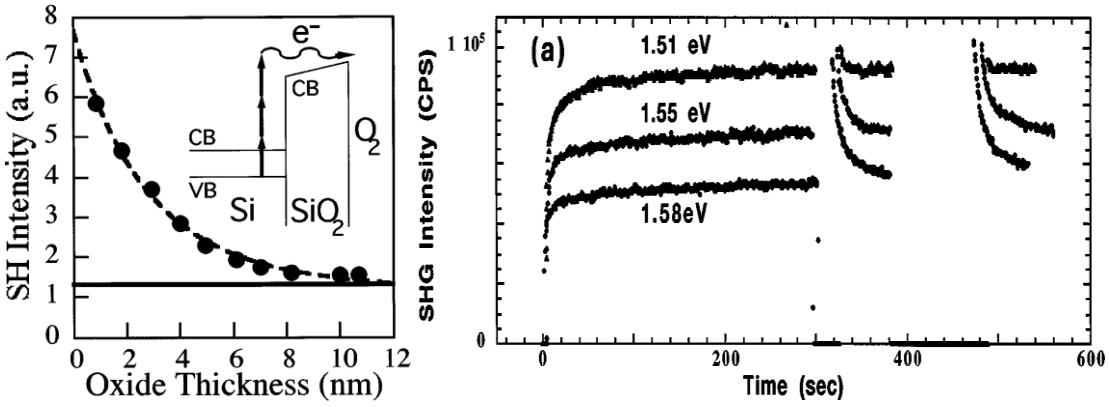

(a) (b)

Figure 2.8. The SHG intensity depends on (a) the thickness of the oxide side (Source: Bloch et al., 1996) and (b) the photon energy (Source: Wang et al., 1998)

In addition, I. Ionica et al studied the characterization of silicon on insulator (SOI) wafers using by Harmonic F1X developed by FemtoMetrix (FemtoMetrix). They analyzed the difference buried oxide (BOX) thickness passivated (thermal oxide) and non-passivated (native oxide) wafers (Ionica et al., 2015) (The clear picture for SOI structure is in Figure 4.13). Their results are shown in Figure 2.9. These figures show us that the passivation samples cause a modification of the interface state (Ionica et al., 2015).

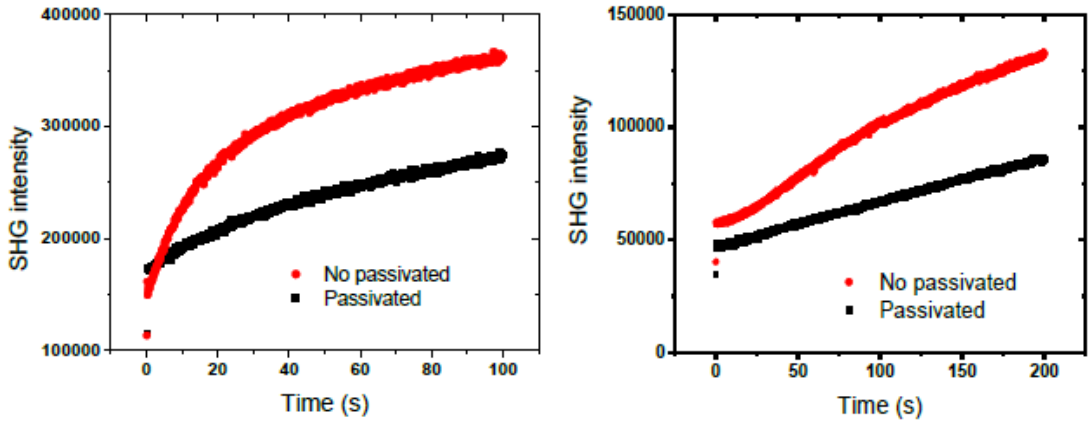

(a) (b)

Figure 2.9. The SHG intensity with 12nm silicon film and 145nm BOX (a) and with 12nm silicon film and 25nm BOX (b) (Source: Ionica et al., 2015)

2.3. Bulk Contribution

The other source of SHG radiation can occur from multipole contribution. Generally, the linear optical susceptibility of crystals has a cubic symmetry because of their isotropic character. However, the high rank of susceptibility tensors such as second and third order nonlinear susceptibilities give rise to anisotropic harmonic generation. In the initial works, the anisotropic effect was not observed. Bloembergen et al. (Bloembergen et al., 1968) showed that the SHG light reflected from silicon crystal was independent of the crystal orientation. However, Tom et al (Tom et al., 1983) used 532 nm to send beam on silicon sample and observed that the SHG light strongly depends on the rotation angle about the surface normal for Si(111) in Figure 2.10 (a) and Si(100) in Figure 2.10 (b) faces. This behavior originates in the structural symmetry of the crystal and of the surface of the sample which is rotated about its surface normal (Tom et al., 1983).

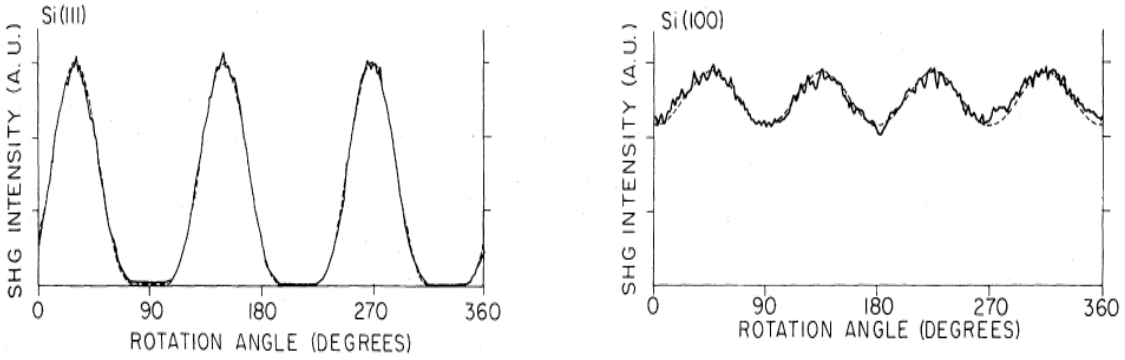

(a) (b)

Figure 2.10. These experiment was done by Tom et al (Tom et al., 1983). They rotated to Silicon about its surface normal from 0 to 360. The intensity of P-polarized SHG signal varies for (a) Si(111) and (b) Si(100) crystal faces under P-polarized incident light.

In Figures 2.10, the SHG intensity varies with the rotation angle of sample about its surface normal. Let us note that this rotation angle will be called azimuthal angle in the following. In this case, and the SHG signal is related to anisotropic effect of the structural symmetry of the crystal. For example, both of the bulk and surface contributions of a (111) crystal face generate an azimuthal dependence. On the contrary, in the case of a (100) crystal face, solely the bulk contribution generates an azimuthal dependence of the SHG signal (Sipe et al., 1987).

At the surface of a medium, the inversion symmetry is broken and the second order nonlinear susceptibility $\chi^{(2)}$ is not zero. However, away from the surface of a centrosymmetric medium, $\chi^{(2)}$ vanishes in the bulk of material and so only the higher order magnetic dipole and electric quadrupole sources produce a nonlinear response. Therefore, the intensity of second harmonic generation can acquire the electric quadrupole and magnetic dipole contributions in the bulk of the crystal. We used a macroscopic theory for bulk Si crystal established by Sipe et al (Sipe et al.,1987). The i'th component of the induced bulk nonlinear polarization can be written

$$\mathbf{P}_i^{2\omega}(\mathbf{r}) = (\delta - \beta - 2\gamma)(\mathbf{E}.\nabla)E_i + \beta E_i(\nabla.\mathbf{E}) + \gamma\nabla_i(\mathbf{E}.\mathbf{E}) + \zeta E_i\nabla_i E_i \qquad (2.44)$$

where the coefficients β, γ, δ and ζ are independent elements of fourth rank tensor which is described by $\chi^{(2),\mathrm{QP}}$. This second-order quadrupole susceptibility depends on material properties and has 81 components. However, only nonzero and independent components of tensor for centrosymmetric materials are $\chi_{iiii}^{(2),\mathrm{QP}}$, $\chi_{iijj}^{(2),\mathrm{QP}}$, $\chi_{ijij}^{(2),\mathrm{QP}}$ and $\chi_{ijji}^{(2),\mathrm{QP}}$ with $i \neq j$. They represent the coefficients β, γ, δ and ζ respectively. The first three terms are isotropic in nature but the fourth one is anisotropic and it is not a scalar (Sipe et al., 1987).

Sipe et al (Sipe et al., 1987) developed a phenomenological model to explain the relationship of crystal symmetries between the SHG intensity and the azimuthal (rotational) angle of the sample. The SHG intensity varies as the azimuthal angle of sample about its surface normal, and the SHG signal is related to anisotropic effect of structural symmetric of the crystal. The symmetry of the azimuthal dependence is different with regard to the crystal orientation of samples. A (100) surface is fourfold (4m) symmetry but a (111) face is threefold (3m) symmetry. Therefore, for Si(100)/ SiO_2 the SHG signal is proportional to $\sin^2(4\varphi)$, corresponding to an eightfold symmetry. However, when the both of the bulk contributions and anisotropic effect are present, the SHG signal gives fourfold symmetry because of this relation: $(\sin(4\varphi) + a)^2$. The relation between the symmetry and S- and P-polarized SHG light intensities can be expressed by a truncated Fourier series (Sipe et al., 1987) (Lüpke et al., 1994):

$$I_{g,p}(\varphi) = \left| \sum_{n=0}^{4} a_n \cos\left(n(\varphi + \varphi_0)\right) \right|^2 \tag{2.45a}$$

$$I_{g,s}(\varphi) = \left| \sum_{n=1}^{4} b_n \sin\left(n(\varphi + \varphi_0)\right) \right|^2 \tag{2.45b}$$

where φ is an azimuthal angle, φ_0 is an arbitrary angle for start measurement, $I_{g,h}(\varphi)$ is the intensity of the SHG signal (g and h represent s and p) and it depends on the azimuthal angle, a_n is a coefficient which leads to the contribution element to second order nonlinear susceptibility. It can be easily understood that the a_0 isotropic coefficient is the surface contribution for the P-polarized SHG intensity. Therefore, it should be the largest coefficient. In addition, a_4 is the anisotropic bulk contribution for a Si(100)/SiO_2 so it leads to fourfold symmetry. Because of the same reason, a_1, a_2 and a_3 are one-, two- and three-fold symmetries. They are zero for ideal Si(100)/SiO_2 interface (Cundiff et al., 1998). They exist if there is a strain on surface, miscut effect or another effects. Thanks to this symmetry ability of SHG light, it is a very promising area to research the material characterization.

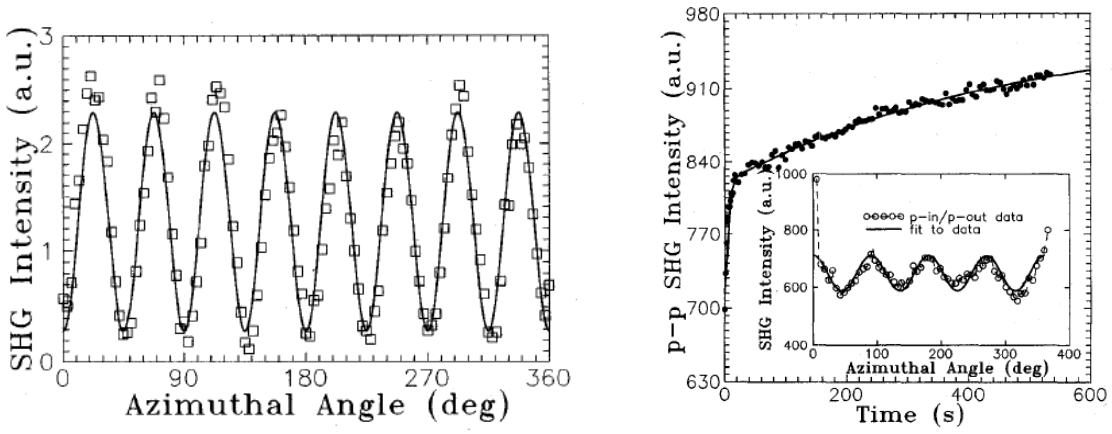

(a) (b)

Figure 2.11. The S-polarized (a) and P-polarized (b) SHG intensity for Si(100) under P-polarized excitation (Source: Dadap et al., 1995).

As an example, Figures 2.11 show the experimental results which the bulk S-polarized and P-polarized SHG signal symmetry are observed as a function of azimuthal angle for Si(100) native oxide crystal by Dadap et al (Dadap et al., 1995). They used an unamplified Ti:sapphire Kerr-lens mode-locked laser which has 800nm of wavelength and 120fs of pulse duration. For S- polarized SHG intensity in Figure 2.11 (a), they

observed that there is no SHG signal comes from surface but there are some signal come from the bulk with an eightfold symmetry because of the form of $\sin(4\varphi)^2$. However, in the case for P-polarized SHG intensity in Figure 2.11 (b), the bulk and the surface electric dipole are present and the intensity varies $(a + \sin(4\varphi))^2$, 'a' represents the contribution of the surface SHG signal. Therefore, the bulk P-polarized SHG intensity changes with a fourfold symmetry.

Separation between the bulk and surface contribution is an encountered problem in the nonlinear optics. Although the bulk of a (100) face is the only one which has an anisotropic response, it is not possible to exactly isolate the bulk and surface. However, there are some ways (Gielis et al., 2008); firstly, the SHG intensity in some specific polarization configuration (S-in P-out, S-in S-out, P-in P-out, P-in S-out) can be measured in different azimuthal angle. With this way, the anisotropic bulk contribution to SHG can be found thanks to symmetrical properties of the bulk. In addition, due to the SHG's high sensitivity of surface, any surface properties can be changed and so it can be easy to distinguish the difference in SHG response. However, for P-polarized SHG intensity, it can be hard to determine small relative changes due to the larger surface contribution (Lüpke et al., 1994). Therefore, the S-polarized SHG intensity can be used to determine them. Lastly, different thin film thickness can be selected to distinguish the interface and bulk.

CHAPTER 3

EXPERIMENTAL SETUP

We applied the given theoretical formulas to model the SHG signal generated from various interfaces. In particular, we applied these formulas for the Si/SiO_2 interface which is of great interest for the microelectronic industry. Measurements are carried out with a commercial equipment called "Harmonic F1X" which is developed by FemtoMetrix, a company based in California. They produced Harmonic F1X for defect control and process uniformity of materials since contaminants such as stains and particles can change the characteristics of subsequent layers (FemtoMetrix). The machine is in development in view of commercialization. The Figure 3.1 given below shows a view of the experimental arrangement inside the Harmonic F1X:

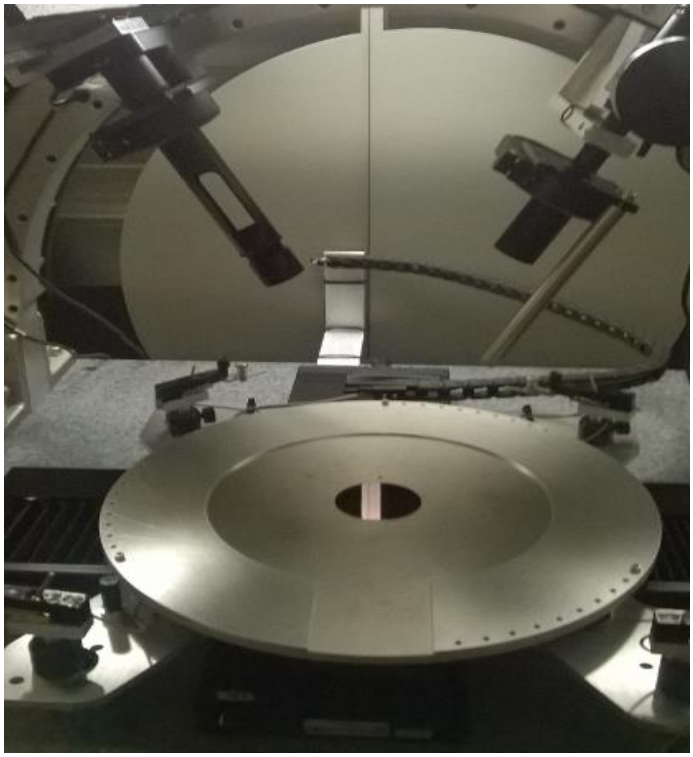

Figure 3.1. The picture of the inside of Harmonic F1X with a 50 mm silicon diameter wafer on the chuck (Details of the machine can be found via (FemtoMetrix))

Two different laser were used during the experiments. For the first laser, the SHG experiments were performed by using a femtosecond laser at 800 nm wavelength which

has a power peak 80kW, an average power 320mW, a pulse duration 95fs and spot size 75μm. After encountering some stability problems with this first laser, we continued to do experiment with the new laser. Thanks to FemtoMetrix Company, the new laser is more effective and stable (the stability problem was investigated also in Section 4.3). The properties of the new laser are shown in Table 3.1.

Table 3.1. The properties of the new laser

Wavelength	**780 nm**
Average power	**460 mW**
Power peak	**80 kW**
Pulse duration	**80 fs**
Repetition rate	**5 MHz**
Laser beam diameter	**2.7 mm**
Focus Length	**150 mm**
Spot Diameter	**50 µm**

Figure 3.2 demonstrates all equipment of Harmonic F1X. Basically, the fundamental light comes from the femtosecond laser to the sample. The spot size of the laser is approximately 50 μm (Damianos et al, 2016). Then, a Half Wave Plate (HWP) is used for changing the polarization state of light. It is placed at the output of the laser which is then focused on the sample surface by a Focus Lens. The reflected SHG signals are collected by Collimator. Then, filters are used to separate fundamental SHG and the original signals. After the filtering system, the SHG signal at 390 nm wavelength is detected by Photomultiplier Tubes (PMT) (Nguyen, 2014).

There are certain experimental parameters for using this equipment (Damianos, 2016). First of all, Angle of Incidence (AOI) $'\theta'$ is very important parameter to measure the SHG intensity. A motorized mechanical mount is used to move the laser such that we can vary the beam angle of incidence from 25° to 65°. In our experiments, we generally use an angle of beam with 45°. Secondly, we measured the SHG intensity according to the input and output polarization which can be varied independently. In the P-polarized (the polarization angle 0°) and S-polarized (the polarization angle 90°) states, the electric field direction of the laser beam is respectively parallel or perpendicular to the surface of the sample. Both of the laser and detector polarization can change between 0° and 90°.

Another critical parameter is the azimuthal angle of the sample. For amorphous materials this is not relevant. However, silicon is crystalline, and the SHG signal may also depend on the angle of crystal with respect the laser plane of incidence. We can rotate manually the sample around the normal axis. For our measurements we obtained silicon wafers with crystal orientations 100. Finally, it is also possible to apply bias between the probe and the chuck. In this work, we applied voltage just for SOI samples.

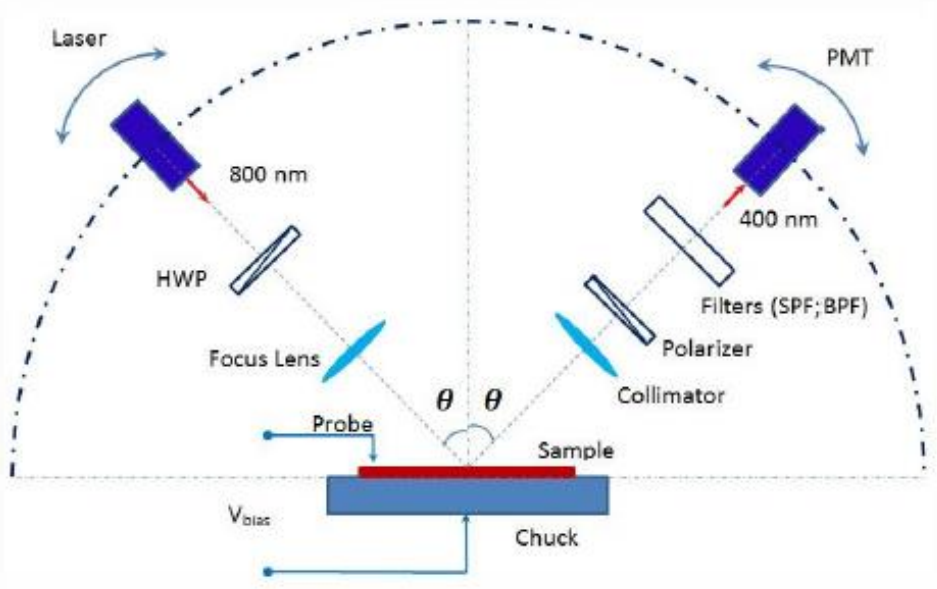

Figure 3.2. The equipment of Harmonic F1X (Source: Damianos, et al, 2016)

CHAPTER 4

EXPERIMENTAL AND SIMULATION RESULTS

This section is about a comparison between the experimental and simulation results of SHG. It shows that there are some dependency factors which have an influence and contribution on the SHG signal such as laser polarization angle, detector polarization angle, angle of incidence light, EFISH (electric field induced second harmonic), azimuthal angle and different oxidation types. To compare with the mathematical model, we use different Si wafers with (100) crystal orientation, together with two kinds of oxides at the silicon surface: very thin (nm) native oxide and thicker (tens of nm) thermal oxide. After, all experiments about Si wafers, silicon-on-insulator (SOI) is used for comparing with Si wafers. The results show that SHG is a very promising tool for characterization of the surface and the bulk of the sample.

4.1. SHG Signal Depends on the Polarization Angle of the Laser and the Detector

Guided by Equation (2.42a) and Equation (2.42b), the input (laser) and output (detector) polarization angles are a critical point of measuring the intensity of the SHG light. If the angle between the electric field direction of the laser beam and the incident plane is 0°, it is called as P-polarized light and if it is 90°, it means that the S-polarized light is perpendicular to the plane of incidence in Figure 4.1. In the experimental results, '-in' and '-out' terms were used to symbolize the polarization angles of input and output signals. Generally, P-in P-out, S-in P-out, P-in S-out and S-in S-out states are commonly used to measure the SHG intensity. The experimental results for Si(100) wafers with thermal and native oxide can be seen in Figure 4.2 and Figure 4.3. Apparently, the SHG intensity of P-in P-out polarizations is maximum comparing to the other polarizations for both experimental results.

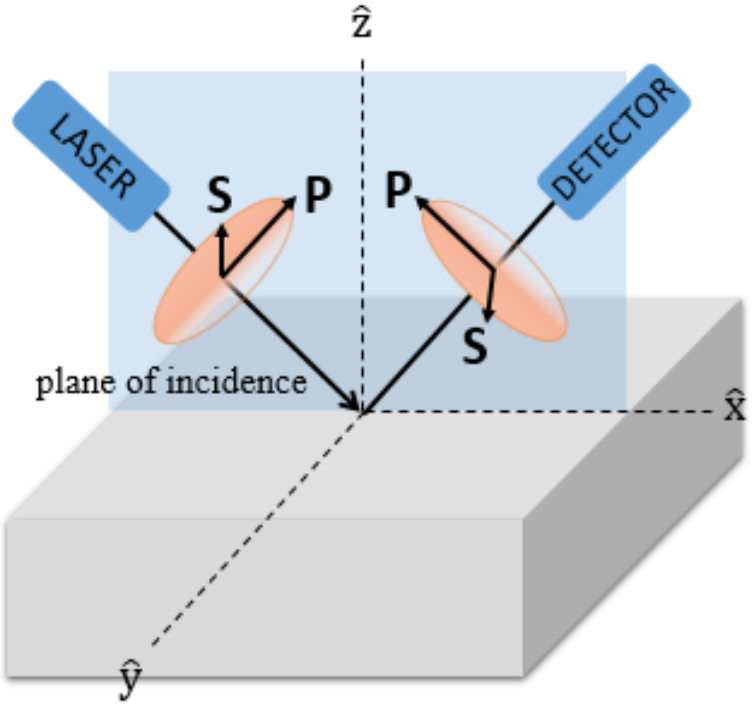

Figure 4.1. The representation of the direction of P and S polarizations

Figure 4.2 shows the impact for the laser and polarization angles on the SHG intensity for Si(100) with thermal oxide. The maximum SHG intensities were measured in P-out state. In our experiment, we generally used P-in P-out state because it produces the strongest SHG signal. Additionally, the SHG intensity is near zero for S-out SHG signal. Because in Equation (2.42a) there is no surface contribution which contribute to SHG intensity for S-out SHG signal if the laser polarization angle (γ_{in}) is at 0° or 90°.

In Figure 4.3, we measured the SHG intensity originating from Si(100) native oxide for different polarization angles of laser and detector during 100 seconds. It has same results with Si(100) thermal oxide: P-in P-out has the maximum SHG intensity and the S-out SHG signal has the lowest intensity under P- and S-polarized incident light. However, for just Si(100) native oxide, the SHG intensity is slowly increasing in time for P-in P-out and S-in P-out configurations. It is because of dc electric field inside Si(100) with native oxide at interface. The detail of this increase on the SHG intensity is explained in section 4.4.

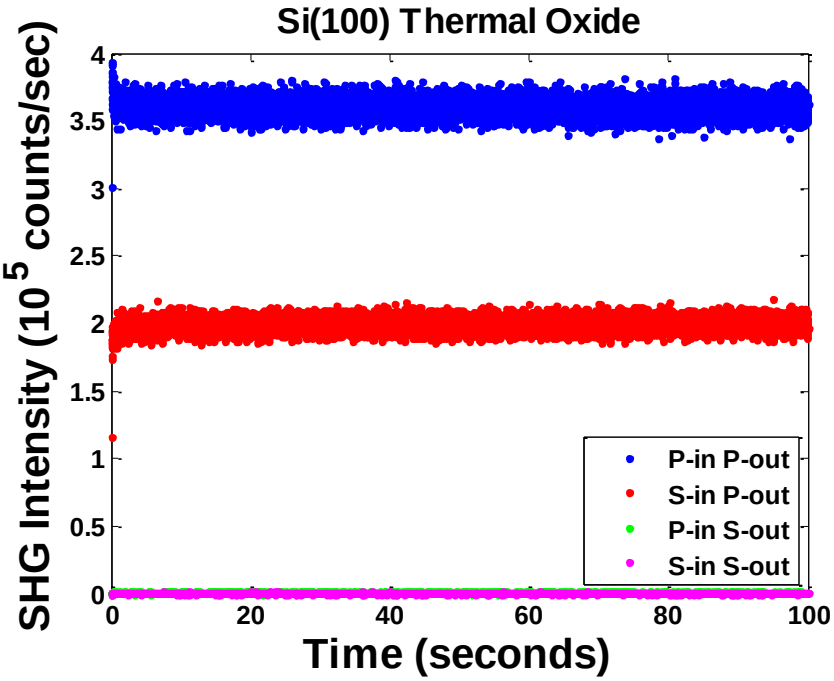

Figure 4.2. The SHG intensities obtained from Si(100) thermal oxide are measured for P-in P-out, S-in P-out, P-in S-out and S-in S-out polarization configurations.

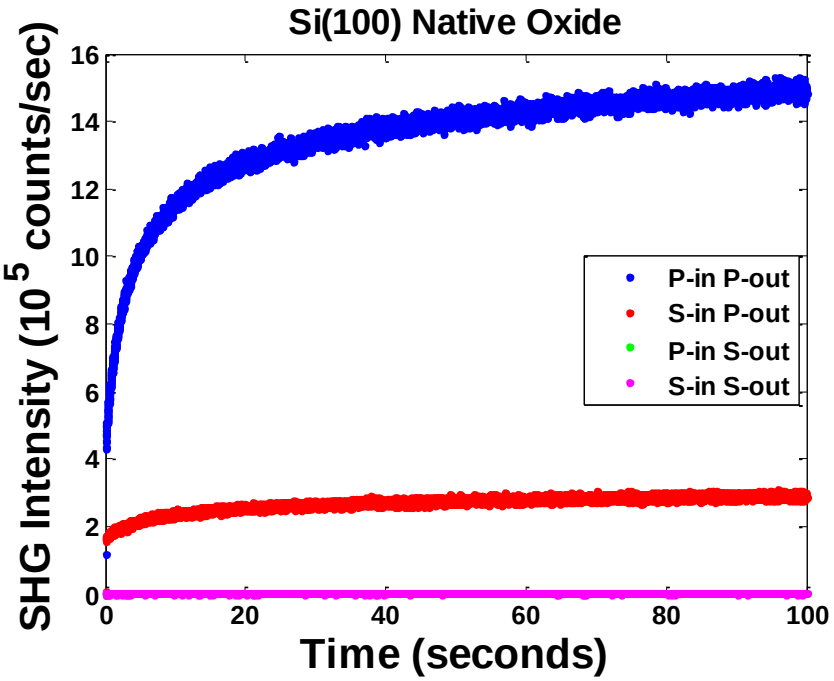

Figure 4.3. The SHG intensities obtained from Si(100) native oxide are measured for P-in P-out, S-in P-out, P-in S-out and S-in S-out polarization configurations.

4.2. Analyzing the Elements of Second-Order Nonlinear Susceptibility Tensor for Silicon

The SHG intensity is directly related to the second order nonlinear susceptibility which was derived in section 2.1.1. For Si(100) crystal faces, there are three independent nonzero tensors; χ_{zzz}, χ_{zii} and χ_{izi} (i=x or y). These nonzero tensor elements can be found by using Equation (2.42a) and Equation (2.42b). These are P- and S- polarized surface-SHG intensities and can be shown

$$I_{sh}^{s}(\gamma_{in}) = K\,|E \sin\gamma_{in}\ \cos\gamma_{in}\ \chi_{izi}|^2 \tag{4.1a}$$

$$I_{sh}^{p}(\gamma_{in}) = K\left|A\cos^2_{\gamma_{in}}\chi_{zzz} - B\cos^2_{\gamma_{in}}\chi_{izi} + \left\{C\cos^2_{\gamma_{in}} + D\sin^2_{\gamma_{in}}\right\}\chi_{zii}\right|^2 \tag{4.1b}$$

where A, B, C, D, E and K coefficients are calculated like in Table 4.1. To find these tensor elements, the least square method was implemented in MATLAB following equations. Both, the experimental and simulation results are shown for P-out and S-out polarization states as a function of the incident polarization angle of light denoted γ_{in} in Figure 4.4 and Figure 4.5. The experiment was done by using Si (100) with thermal and native oxides. In Table 4.1, dielectric constants for SiO_2 are real for two different frequencies under consideration because it is transparent at both wavelengths. On the contrary Si is absorbing at both 800nm and 400nm wavelengths, and its dielectric constant is therefore complex (Palik, 1997).

Table 4.1. Dielectric constants for Si and SiO_2

Wavelength	**SiO_2**	**Si**
800 nm	1.4533^2	$(3.6801 + 5.22 * 10^{-3} * i)^2$
400 nm	1.4701^2	$(3.5832 + 2.96 * 10^{-1} * i)^2$

We have arbitrary units for the tensor elements because SHG intensity is not absolutely calibrated. As a consequence, we can only deduce the two ratios χ_{zzz}/χ_{zii} and χ_{izi}/χ_{zii} from the experimental data. Therefore, we determined the ratios from the comparison between experiment and the SHG model. As shown on Figure 4.4 and Figure 4.5, we succeeded in obtaining good agreement between experimental measurements and

model. Furthermore agreement is obtained for a given set of the two ratio and we've been able to deduce their values for Si(100) with thermal oxide: χ_{zzz}/χ_{zii}=-61,10 and χ_{izi}/χ_{zii}=-0,80 in Figure 4.4.

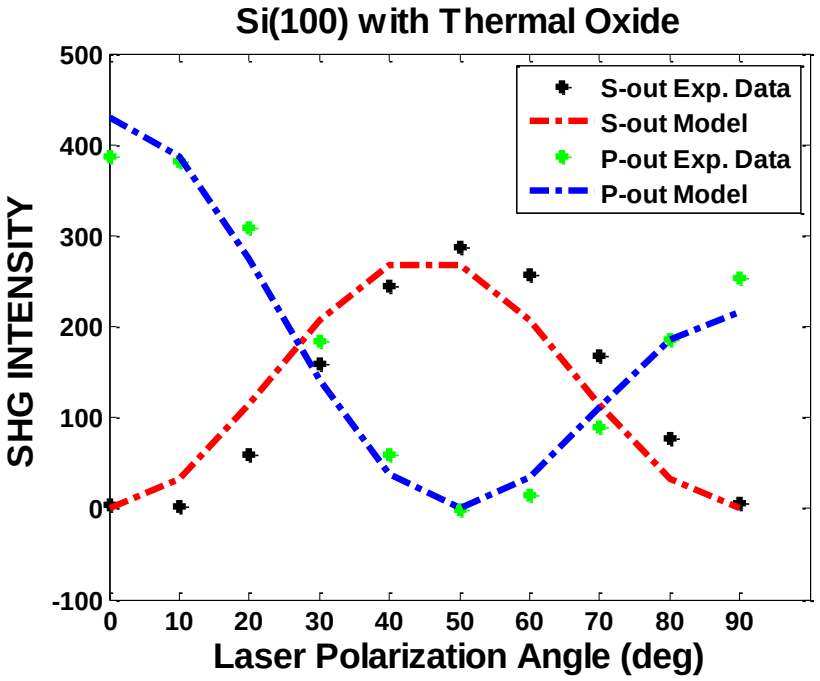

Figure 4.4. Experimental and simulation results for Si(100) with thermal oxide

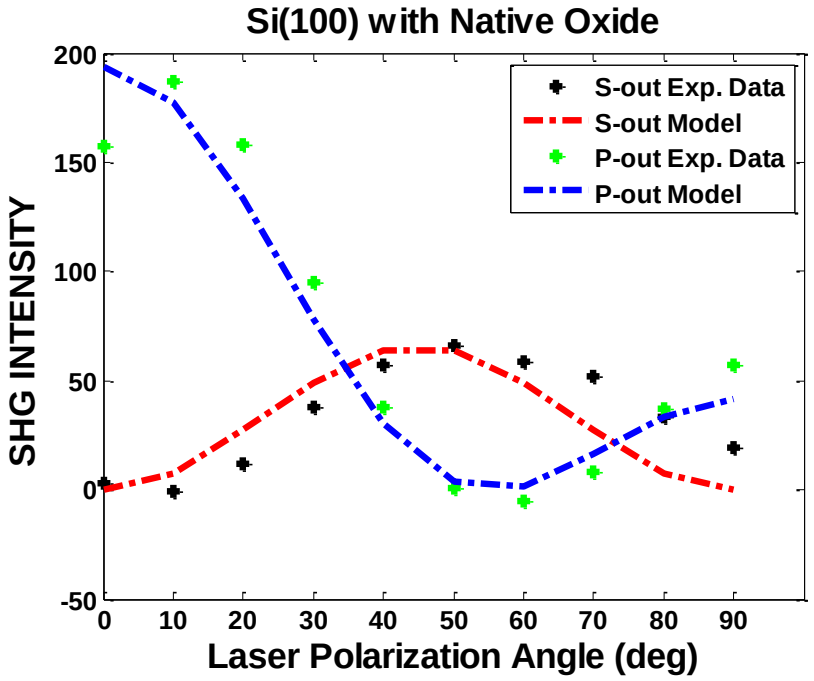

Figure 4.5. Experimental and simulation results for Si(100) with native oxide

In addition, the SHG signal from Si (100) native oxide was measured as a function of laser polarization angle for P-out and S-out states. We observed that oxidation types also have a very important influence on the SHG response curve. Therefore, the second order nonlinear susceptibility ratios are not the same for the two oxide types. Figure 4.5 shows that the agreement is still provided we take other values for the two ratios which are here: χ_{zzz}/χ_{zii}= -75,5 and χ_{izi}/χ_{zii}= -0,90.

In summary, the results show us the tensor elements can be found using the phenomenological model of SHG, as described in section 2.1.2. Another point about these tensors, χ_{zzz} has the strongest contribution to SHG, also the tensor element of χ_{izi} and χ_{zii} is nearly equal each other and so have same contributions to SHG.

4.3. SHG Signal Depends on Angle of Incidence

SHG signal strongly depends on the angle of incidence (AOI). This dependence comes from the medium refractive indices of n_1, n_2 ($n_{1,2} = \sqrt{\varepsilon_{1,2}(\varphi)}$) in Equation (2.41). Due to reflectivity coefficient for different interfaces, there is a definite angle that gives the maximum SHG intensity. Theoretically, this angle is not affected by the nonlinear susceptibility ratios, these ratios just change the intensity curve of SHG light. The numerical results of the angular dependence of the SHG intensity were simulated according to P-in P-out, S-in P-out, P-in S-out and S-in S-out polarization configurations at Si/SiO_2 interface. They are presented in Figure 4.6.

Figure 4.6 provides that the SHG intensity appears at P-in P-out and S-in P-out polarizations and it has an intensity of nearly zero at P-in S-out and S-in S-out polarization states. This observation is in good agreement with phenomenological model of SHG. Indeed, because of the sine and cosines multiplication in Equation (2.42a), the SHG intensity for S-out is always zero according to the incidence polarization angles of γ_{in}=0°,90°. While the maximum SHG intensity for P-in P-out polarization is at the angle of 61°, S-in P-out polarization intensity is at the angle of 69°. Increasing the ratio of χ_{zzz}/χ_{zii} leads to an increase in the SHG intensity of P-in P-out. The ratio of χ_{izi}/χ_{zii} directly affects the S-out SHG intensity.

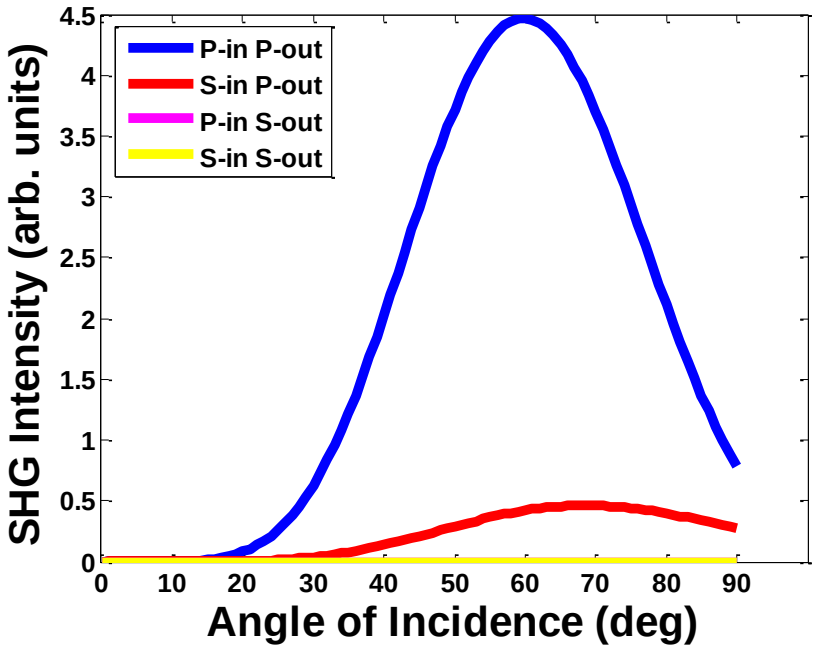

Figure 4.6. The SHG intensity, which was derived by using phenomenological model of Sipe and Mizrahi (Mizrahi & Sipe, 1988), was simulated with nonlinear susceptibility ratio χ_{zzz}/χ_{zii}=-61,10 and χ_{izi}/χ_{zii}=-0,80 at Si/SiO_2 interface in different angle of incident light

Afterwards, to compare the simulation results with experimental results, we used two different oxidation types for Si(100): native and thermal. The results are shown in Figures 4.7. In this experiment, we measured P-in P-out SHG intensity while we were rotating our samples about its surface normal (azimuthal angle) for the degree of 45°, 90°, 135° and 180°. For both results, at 0°, 90° and 180° the SHG intensities overlapped, and they also overlapped for the degree of 45° and 90° with less SHG intensity in Figures 4.7. This is normal and proves that the experimental setup with the new laser is perfectly reliable.

In addition, we could not observe the maximum angle of incidence for Si(100) native oxide which gives maximum P-in P-out SHG intensity like Si(100) thermal oxide. It is around at 52° for Si(100) thermal oxide in Figure 4.7 (a). Therefore, we decided to try the other polarized fundamental and SHG light; such as P-in S-out, S-in S-out and S-in P-out at the same azimuthal angle 0°. The result for P-in S-out was same with Figure 4.7 (b). However, the SHG intensity for S-in S-out and S-in P-out had same graph but with different shape from the P-in P-out graph. It is shown in Figure 4.8 for S-in P-out SHG intensity. The maximum SHG intensity is at 50°for Si(100) native oxide.

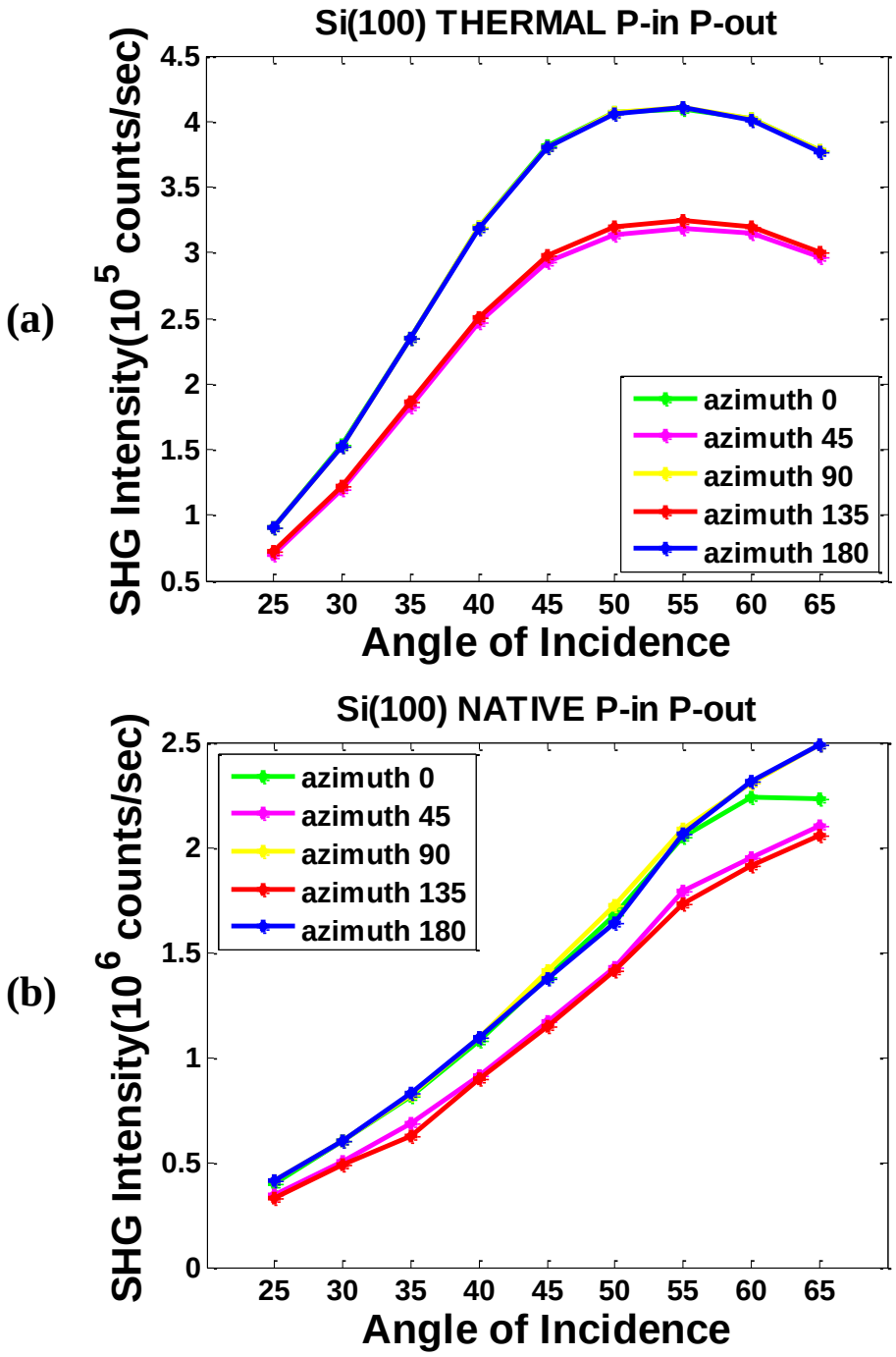

Figure 4.7. The results for P-in P-out SHG intensity for Si(100) thermal oxide(a) and for Si(100) native oxide (b) as a function of the angle of incidence in different rotational angle

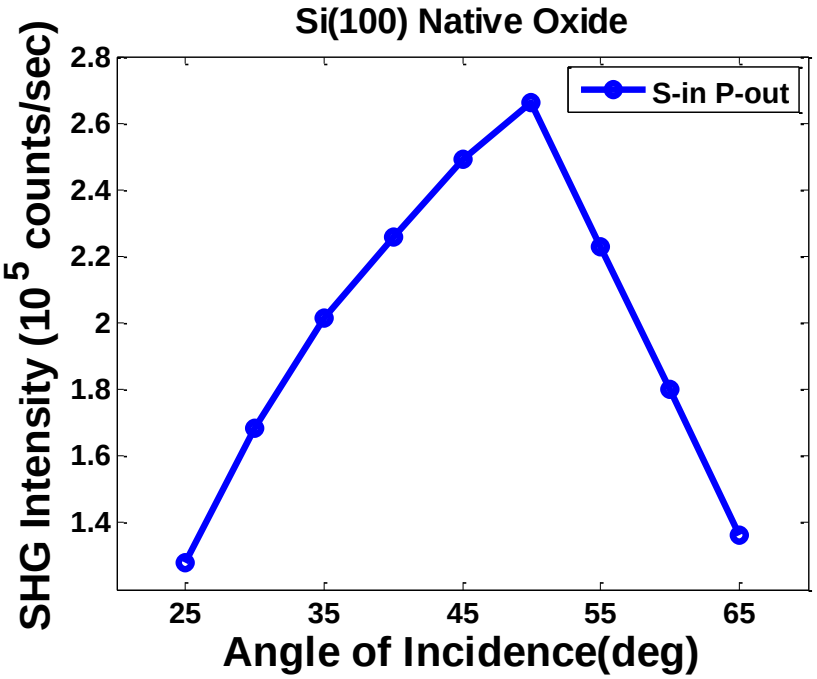

Figure 4.8. The S-in P-out SHG intensity as a function of the angle of incidence for Si(100) native oxide

The differences of SHG intensity for different polarization configurations for Si(100) native oxide can be caused by the static electric field at interface or it can be possible to see the maximum angle of incidence after 65° but the machine allows us to measure from 25° to 65°.

4.4. SHG Signal Depends on EFISH

The SHG signal is generated at Si/SiO_2 interface due to the broken inversion symmetry and has also contribution from the dc electric field at the interface. At Si/SiO_2 interface, the pulsed laser irradiation produces electron-hole pairs in Si region, some of the electrons acquire enough energy to overcome the barrier at the Si/SiO_2 interface and they are injected into the oxide surface. Because of the separation of electrons, an electric field is created at interface. This electric field induced second harmonic (EFISH) is third order process and can be described by

$$I^{2\omega}(t) \propto \left| \chi^{(2)} + \chi^{(3)} E_{dc}(t) \right|^2 . (I^{\omega})^2 \qquad (4.2)$$

This equation explains the sensitivity of SHG signal in terms of the interface and oxide defects (Ionica et al., 2015).

When we measured the SHG intensity of Si(100) native and thermal oxide for different polarization angles, we observed that the SHG intensity from Si(100) with native oxide increases in time as in shown in Figure 4.9. Whereas the same experiment was done for also the thermal oxide one but the SHG intensity does not increase or decrease in time. We believed that it is caused by different thickness of oxides. Because the thickness of thermal oxide is very thick with regard to native oxide. Therefore, we cannot see long period of saturation like native oxide. However, for native oxide, $E_{dc}(t)$ can saturates and starts compensating the initial electric field after a long time. We can also say that the direction of dc electric field is opposite to the initial field because of the direction of increment, so it means that the electrons in silicon region injects into the oxide region.

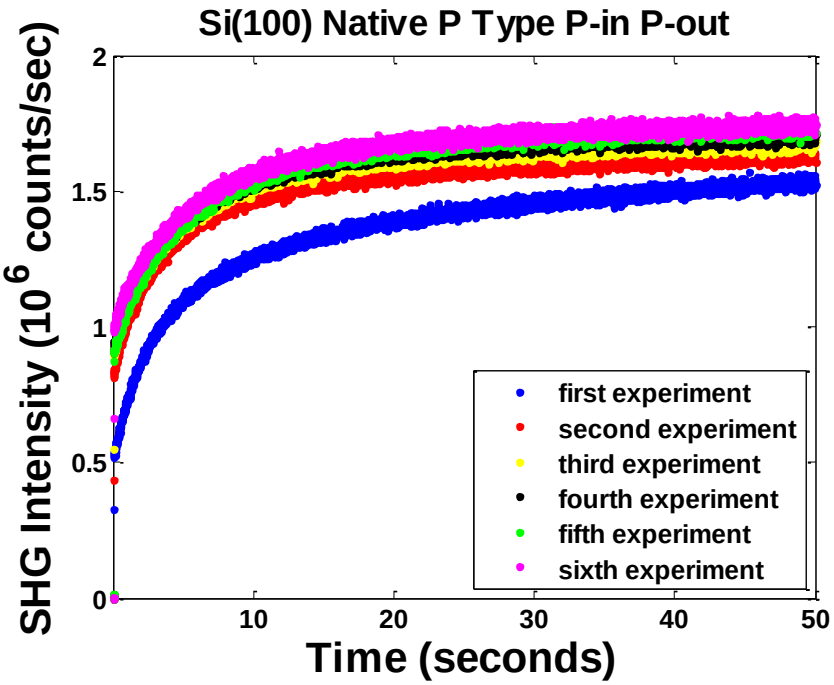

Figure 4.9. The graph of P-in P-out SHG intensities vs time for Si(100) native oxide

In Figure 4.9, we repeated the same experiment six times at each five minutes for P-in P-out SHG intensity for Si(100) native oxide. The aim for this experiment is to check whether the SHG intensities are same every experiments for Si(100) native oxide. We observed that the starting and final point of the SHG intensity increases for every next experiment. This proves this charging effect is originated by dc electric field inside.

4.5. SHG Signal Depends on Oxidation

Silicon can exist with its oxide, and oxidation method is also a critical point for SHG intensity. We used two different types of oxidation: native and thermal. SiO_2 is a native oxide of Si. Thermal oxidation of silicon is that the SiO_2 is heated to a temperature between 800°C and 1200°C. The result is that thermal oxide is thicker than native one (a few nm). Figure 4.10 shows a comparison between thermal and native oxide with the crystal orientation (100) for Si. Native oxide sample has a higher intensity than the thermally oxidized silicon.

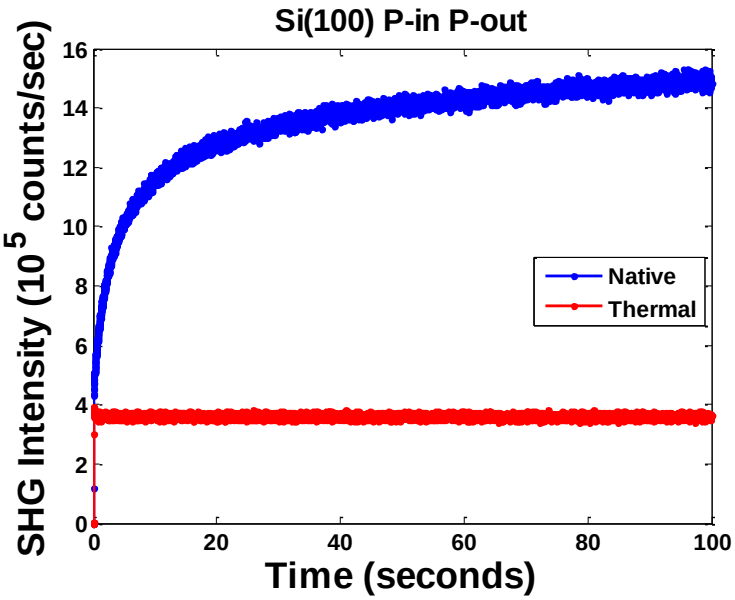

Figure 4.10. The SHG intensity vs laser polarization angle for Si(100) native and thermal oxide

4.6. SHG Signal Depends on Azimuthal Angle

In the experimental results, we observed differences in the SHG intensities when silicon wafers were rotated about its surface normal. It is an interesting result for silicon because silicon is centrosymmetric material. However theoretically, the induced polarization is also related to the position of the electric field. Therefore, because of that reason the SHG intensity can depend on also the rotation of sample. We performed the experiment to see the dependency of azimuthal angle (the azimuthal angle is the angle between the plane of incidence and the crystal axis.) for samples. This experiment can

give information about the crystal orientation of samples and also to determine the surface and bulk contributions to SHG.

Si (100) wafers were rotated manually from 0° to 180° for native and thermal oxide types. The SHG intensity was measured with respect to P-in P-out and P-in S-out polarization states. Figure 4.11 (a) and (b) belong to the results of Si (100) with thermal oxide for P-in P-out and P-in S-out SHG intensities. Also, Figure 4.12 (a) and (b) are for Si (100) with native oxide in same polarization order like thermal one. The finding was similar to the work by Tom et al. as in Figure 2.10 and Dadap et al. Figure 2.11. If we examine the results, generally thermal and native oxide have same shape of graph for same polarizations. However, we observed different symmetry for different polarized SHG signal. If we extend the azimuthal angle's range from 0° to 360° because it is symmetric, it can be observed fourfold symmetry for the P-out SHG intensity and eightfold symmetry for the S-out SHG intensity. We have already known that our silicon wafers should have fourfold symmetry because of that the crystal orientation of its surface is (100). Therefore, this result provides that SHG signal is related to directly crystal orientation of sample.

In addition, the reason for observing different symmetry properties depends on contribution of the bulk electric quadrupole and the surface electric dipole. If we summarize total intensities of P-out and S-out SHG intensities for (100) crystal orientation as a function of azimuthal angle, they would be like following equations as mentioned before in Equations (2.45) ($\varphi_0 = 0$):

$$I_{p,p}(\varphi) = \left| \sum_{n=0}^{4} a_n \cos(n\varphi) \right|^2 \tag{4.3a}$$

$$I_{p,s}(\varphi) = \left| \sum_{n=1}^{4} b_n \sin(n\varphi) \right|^2 \tag{4.3b}$$

(a)

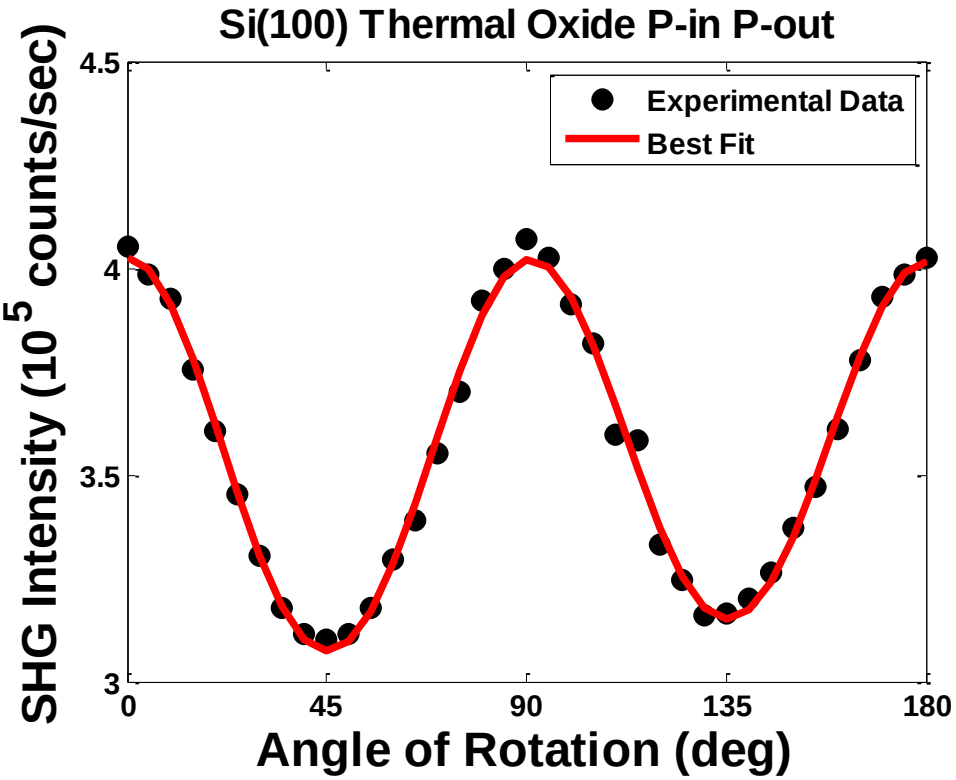

(b)

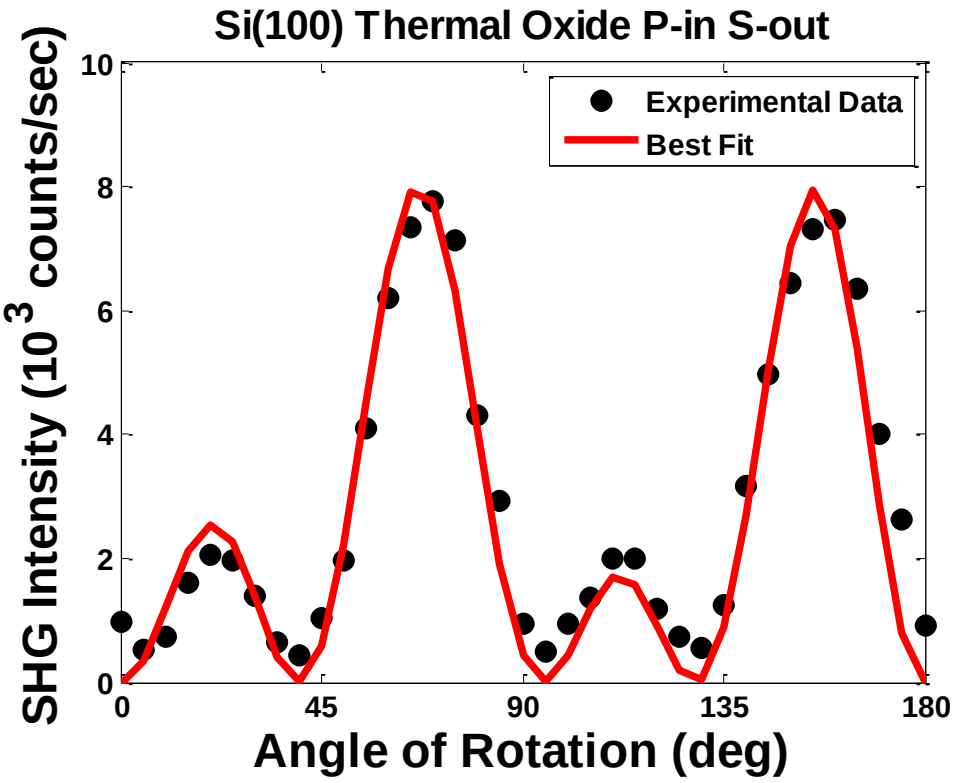

Figure 4.11. (a) The P-in P-out SHG intensity and (b) the P-in S-out SHG intensity were measured as a function of angle of rotation (azimuthal angle) for Si(100) with thermal oxide

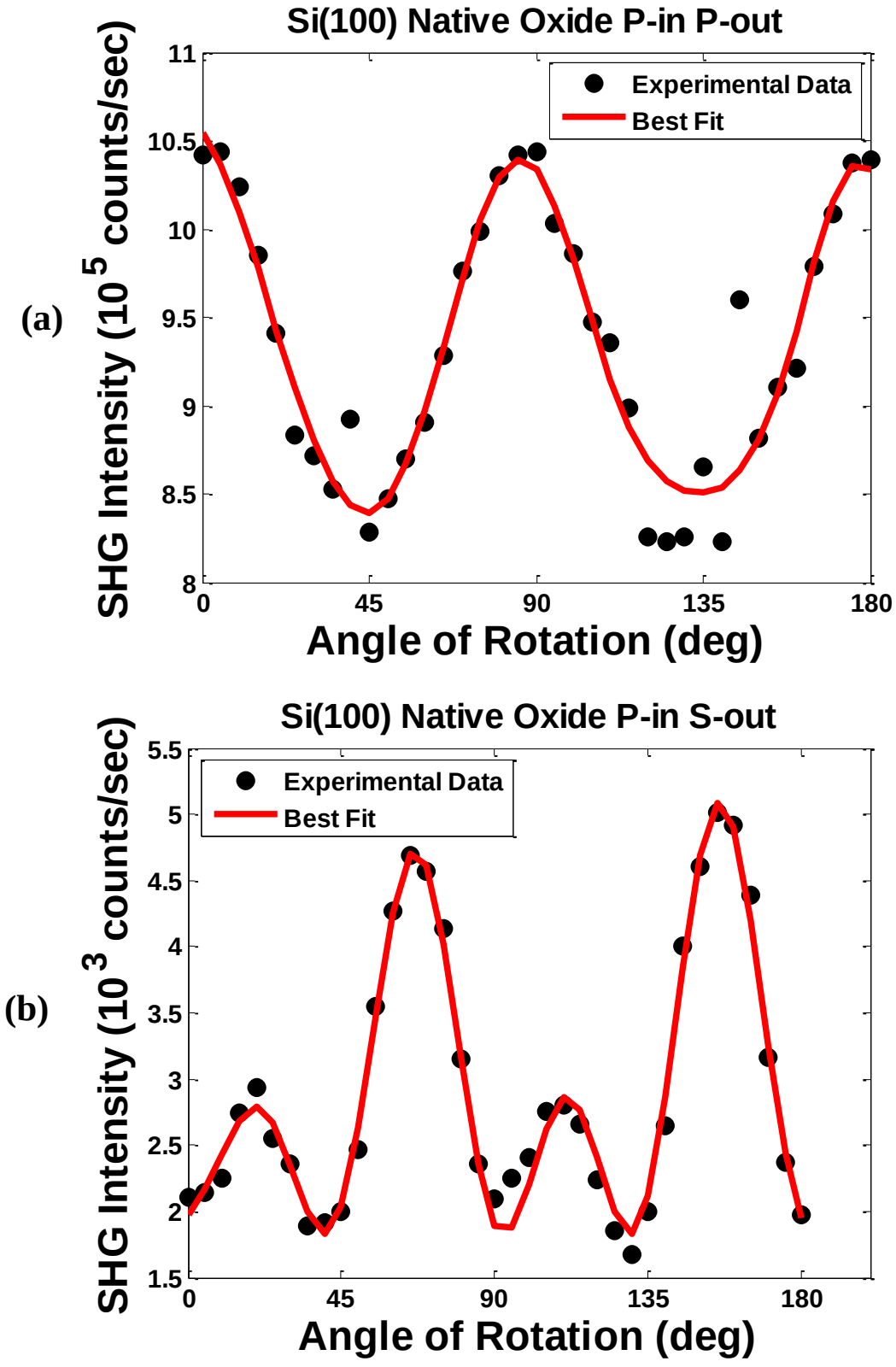

Figure 4.12. (a) The P-in P-out SHG intensity and (b) the P-in S-out SHG intensity were measured as a function of angle of rotation (azimuthal angle) for Si(100) with native oxide

We deduced the a_n and b_n Fourier coefficients using Equations (4.3) to fit the experimental data. The values of Fourier coefficients for Si(100) with thermal oxide are demonstrated in Table 4.2. We find that the a_0 is the largest Fourier coefficient. This is theoretically expected (Sipe et al., 1987) because we know that the a_0 coefficient is isotropic surface contribution and dominant the other terms for the P-out SHG intensity. In addition, the a_4 coefficient, which mainly arises from the bulk quadrupole sources, is relatively large. Therefore, the P-out SHG intensity varies as a function of azimuthal angle with fourfold symmetry, as $(a_0 + a_4\cos(4\varphi))^2$ in Equation (4.3a). The other a_1, a_2 and a_3 coefficients are partly small, this can be because of the large surface contribution of a_0. When we examine eightfold symmetry for the S-out SHG intensity, it means that there is no dominant isotropic surface contribution. Therefore, the b_4 coefficient is the largest one in all Fourier coefficients

Table 4.2. The Fourier coefficients were fitted to the measured data of P-in P-out and P-in S-out the SHG intensity for Si(100) with thermal oxide

n	P-in P-out ($\boldsymbol{a_n}$)	P-in S-out ($\boldsymbol{b_n}$)
0	595.97	-
1	-2.28	29.53
2	0.04	-2.58
3	2.66	8.57
4	38.14	-67.34

For determining the Fourier coefficients for Si(100) with native oxide, we could not fit properly the experimental data using with Equations (4.3) for P-in S-out polarization state. Therefore, in order to find a best fit for the experimental data, we used more general expression of truncated Fourier expansion which given by Bottomley et al. (Bottomley et al., 1993). It is shown as

$$I_{g,f}(\varphi) = \left| \sum_{m=1}^{4} [a_m \cos(n(\varphi + \varphi_0)) + b_m \sin(n(\varphi + \varphi_0))] \right|^2 + h \qquad (4.4)$$

where g and f represent s or p polarization states. The surface and bulk contributions are calculated in this relationship: $c_m = {a_m}^2 + {b_m}^2$, is defined in (Bottomley et al., 1993).

The c_m coefficients are shown in Table 4.3 for Si(100) with native oxide. The coefficient h is the largest one in the results of P-in P-out state. It shows that again the surface isotropic contribution is dominant the other terms. However, for P-in S-out state, c_4 is the largest one as in the result of the thermal oxide one. The other coefficient c_1, c_2 and c_3 shows the other facial orientation of the bulk. In our case, we do not have any specific information about the native oxide sample. The only thing we know that the thickness of the native oxide one is higher that the thermal oxide one. Therefore, it can be said that when the thickness of oxide becomes smaller, the surface sensitivity of SHG increases.

Table 4.3. The Fourier coefficients were fitted to the measured data of P-in P-out and P-in S-out the SHG intensity for Si(100) with native oxide

	P-in P-out	P-in S-out
$\boldsymbol{h}$	839370	1829
$\boldsymbol{c_1}$	79090	2044
$\boldsymbol{c_2}$	29150	2610
$\boldsymbol{c_3}$	85260	1079
$\boldsymbol{c_4}$	12140	2721

As a summary, the SHG signal strongly depends on the azimuthal angle of the sample. We showed that this dependency can be used to identify the crystal orientation of the sample and determine the surface and bulk contributions to SHG intensity.

4.7. SHG Results Compare with Silicon On Insulator (SOI)

After getting some information about sample silicon wafers, we continued to do experiment with Silicon on Insulator (SOI). Therefore, we can compare SOI's results with our previous result about silicon wafers. Figure 4.13 illustrates the sample structure of SOI. It consists of a thin Si(100) film on the top of buried oxide (BOX) which is attached onto a Si(100) substrate. The upper Si films has been etched such that we are left with squares of SOI of size 3.0 x 3.0 mm^2 like islands. Between these squares of SOI, the structure is only constituted of an SiO_2 layer on top of Si wafer. The distance between two SOI islands is 2 mm. Thanks to separate structures of BOX and SOI; we can observe both regions.

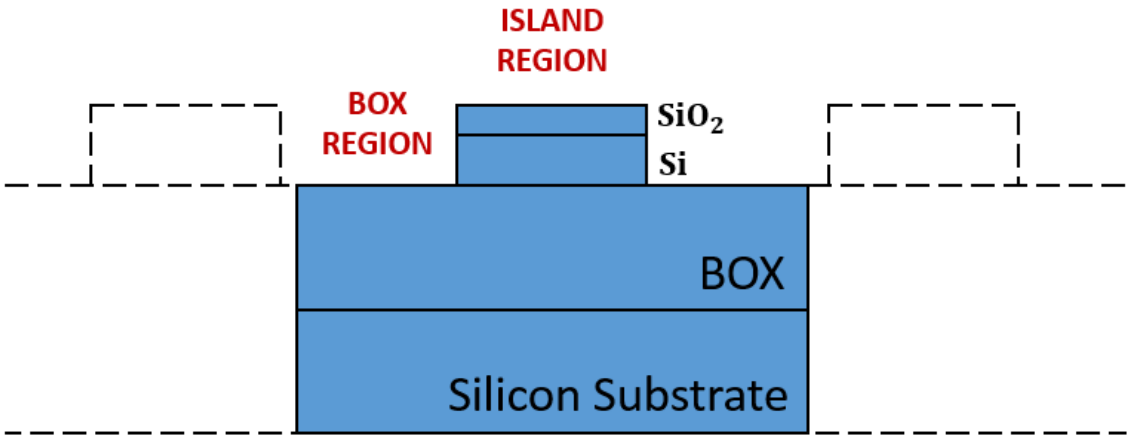

Figure 4.13. The structure of SOI

In our experiment, the oxide type of Si film is non-passivated (native). The thickness of film and BOX is 88nm and 145nm, respectively. The SHG signal is obtained 45° angle of incidence for P-in P-out and P-in S-out. We performed the experiment to see the dependency of rotational angle and the applied external electric field for SOI on studying the SHG signal.

To check the hypothesis that we should get same rotational effect on SHG signal on rotating SOI. We investigate the experiment for island and BOX region to compare the results. We call ISLAND the regions and BOX the regions where the upper silicon has been etched, i.e. outside the squares of SOI in Figure 4. 13. We measured P-in P-out and P-in S-out SHG signal comes from ISLAND and BOX in Figure 4.14, and we rotated the sample about its surface normal from 0° to 90°. The results were surprising because even for multinterface structure, the SHG intensity varies depending on the crsytal orientation of sample same like silicon wafers in Figure 4.11 and Figure 4.12. For example for P-in P-out SHG signal for ISLAND and BOX region of SOI in Figure 4.14, the SHG intensity varies with fourfold symmetry if we extend to azimuthal angle from 0° to 360°. This is again related to the form of $(a_0 + a_4\cos(4\varphi))^2$ in Equation (4.3).

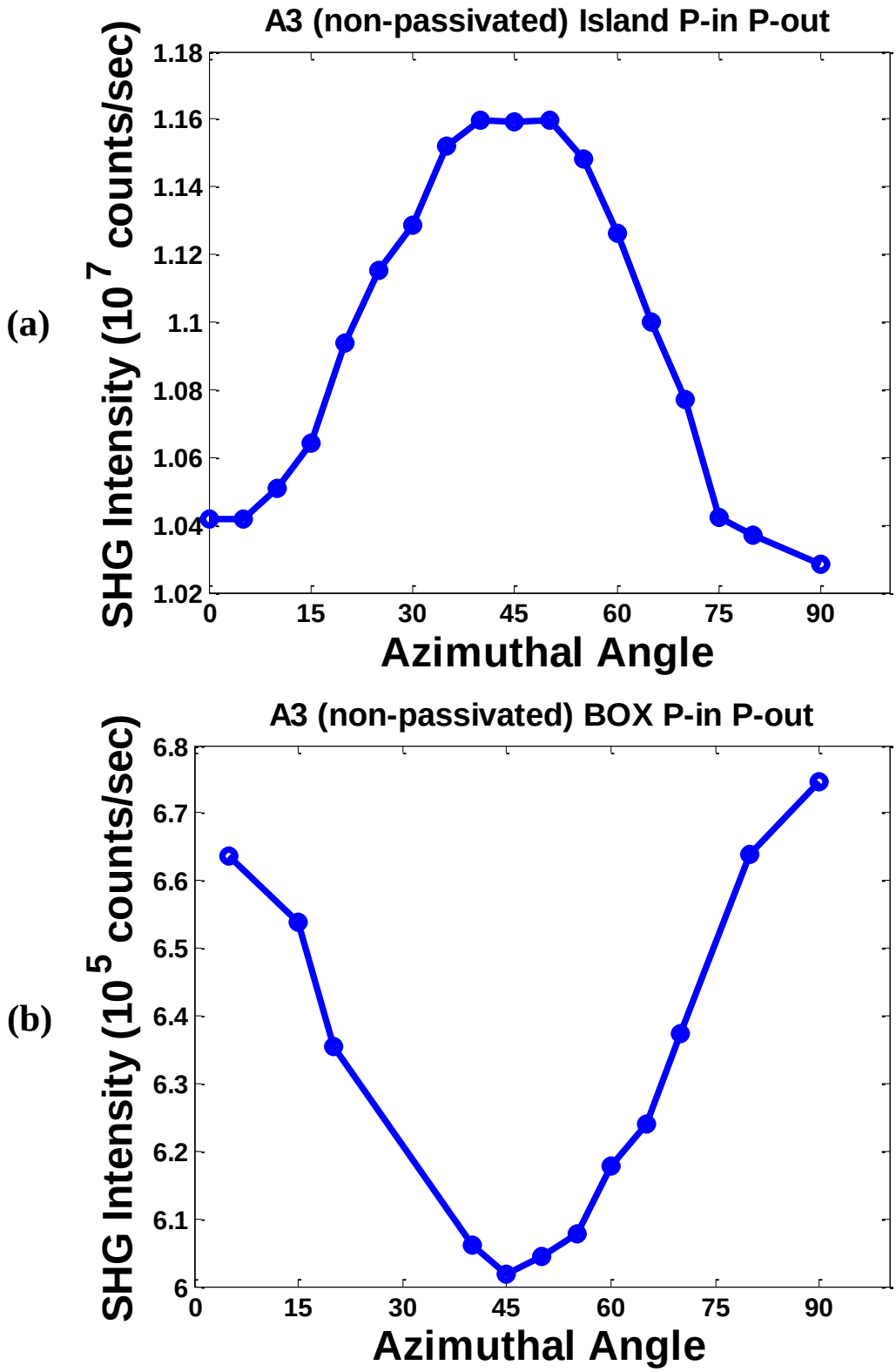

Figure 4.14. The P-in P-out SHG intensity was measured as a function of azimuthal angle for (a) ISLAND region and (b) BOX region

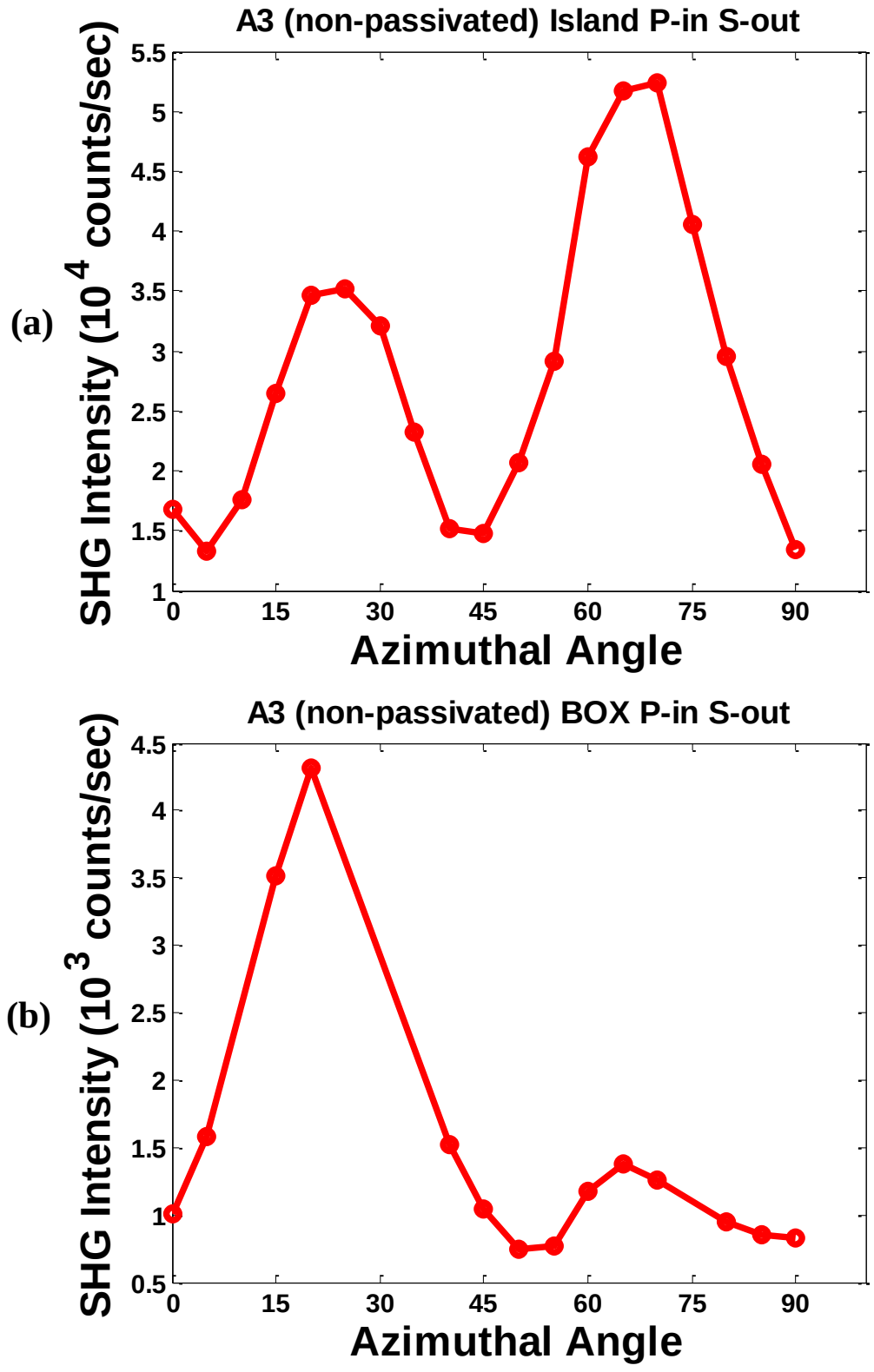

Figure 4.15. The P-in S-out SHG intensity was measured as a function of azimuthal angle for (a) ISLAND region and (b) BOX region

Additionally, we measured SHG signal generated from ISLAND and BOX for P-in S-out intensity in Figure 4.15 (a) and (b). The SHG intensity varies with eightfold symmetry for both cases if we again extend to azimuthal angle from 0° to 360°. In this case, there is no isotropic contribution to the SHG intensity which comes from surface or interface regions. Therefore, the form of the SHG intensity is $\sin(4\varphi)^2$ like in Equation (4.3).

In addition, second harmonic optical technique is used to investigate the quality of buried surfaces and semiconductor interfaces. Electric field at the interface of Si/ SiO_2 varies with time. This helps us to understand the influence of the quality properties of interface.

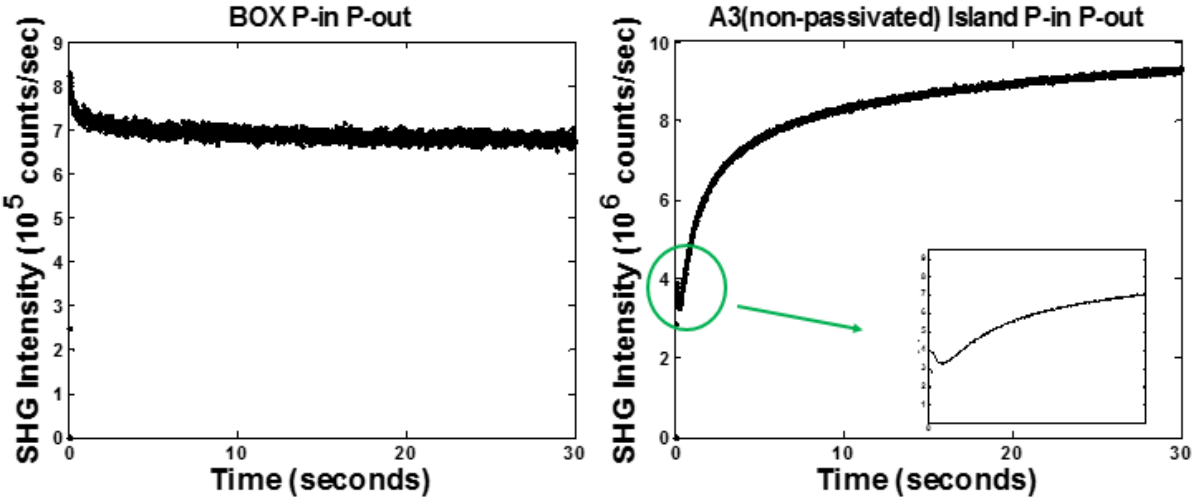

(a) (b)

Figure 4.16. The P-in P-out SHG intensity were measured in time for BOX (a) and ISLAND (b) regions of SOI

The experimental results in Figure 4.16 give us some information to estimate the direction of the electric field inside. In Figure 4.16 (a), the SHG signal generates from BOX region, and typical BOX surface has residual positive charges. The thickness of BOX is thicker than 10 nm. Therefore, the electrons at silicon surfaces cannot reach the oxide surface (Bloch et al., 1996). (This relation between the thickness of the oxide surface and the SHG intensity was shown in Figure 2.8 (a)) When the light irradiated to BOX region, the SHG intensity decrease a little in time. However, after a while, the electric field inside and the initial electric field starts compensating and the time dependent electric filed become constant. We believed that the decrease at the beginning is caused by the opposite direction of the electric field inside (Park et al., 2009).

Afterwards, we measured the intensity of generated second harmonic light from ISLAND region and we detected larger SHG intensity than the result of BOX region in Figure 4.16 (b). This is because of that second harmonic light is generated from more than one interface. In addition, the SHG intensity increases slowly like our previous experiment for Si(100) native oxide in Figure 4.10. However, the beginning of the shape of graph until 1 second, we observed a decrease and increase on the SHG intensity. We estimated that this is caused by the total of the electric field inside. We should call like the total of the electric field inside because there are more than one dc electric fields inside the SOI. One of them is between Si-sub and BOX, another is between BOX and Si film, the other is Si film and its native oxide. So, at the beginning, we can say that the direction of the inside electric field is opposite to the initial field. Then they become equal at the level of minimum SHG intensity. After that, the time dependency SHG intensity increases slowly until it saturates.

In addition, we applied different voltages to the Si-substrate to see the impact of dc electric field. We apply different voltage on the direction of surface, so it effects only to dc electric field. We performed this experiment for -30V, -15V, 0V, 15V and 30V in Figure 4.17. The results show us that the SHG intensity at -30V is larger than the other applied voltage. This can be caused by the direction of electric field inside.

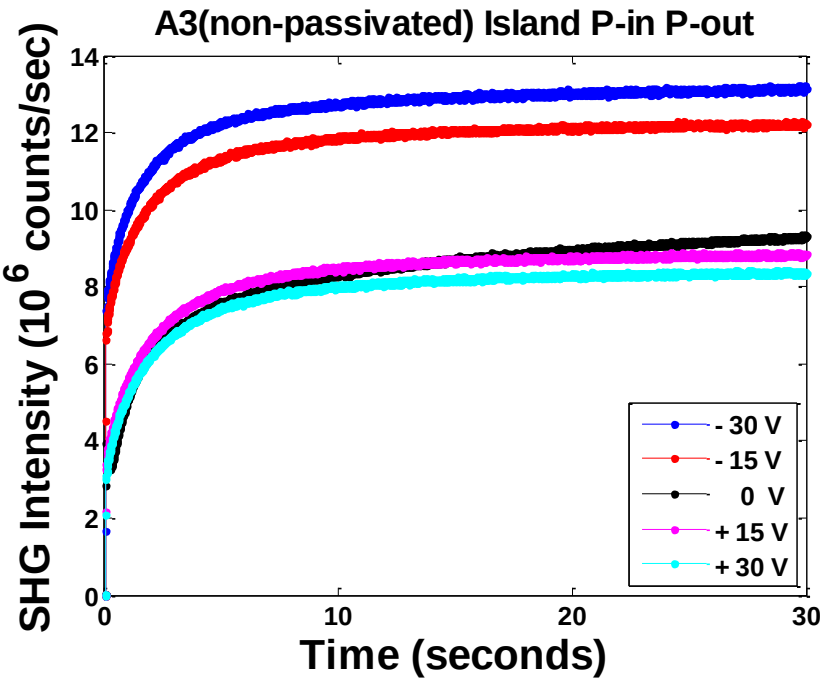

Figure 4.17. Different voltages (-30V, -15V, 15V, 30V) were applied on ISLAND region of non-passivated (native) SOI sample.

CHAPTER 5

CONCLUSION

In summary, we demonstrated that SHG is an effective, non-destructive and contactless characterization method in microelectronic industry. In this thesis, different materials were used to observe SHG signal and to develop a suitable characterization model.

Figure 5.1. The structure of Glass + TiO_2 (with 250nm thickness)

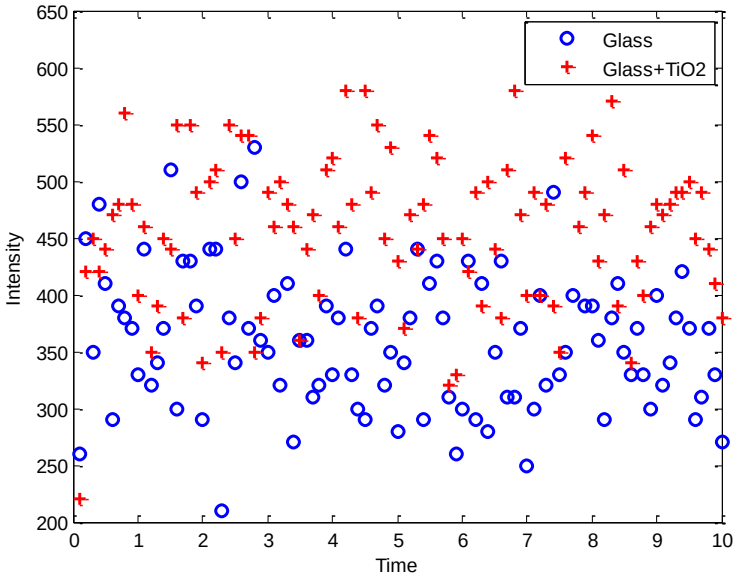

Figure 5.2. The SHG intensity vs time for Glass and Glass + TiO_2 (with 250 nm thickness)

Firstly, we started our research with simple glass substrate. The idea was to test the model on the simple glass/air interface which should be able to generate a SHG signal. Theoretically, SHG signal must occur at air/glass surface because of the breaking of the centrosymmetric at the interface. However, we could not find any further information

about this phenomenon in the literature for glass/air interface, it is probably because of that the SHG signal from glass is expected to be very small. However, we observed a SHG signal from air/glass interface, although it is preliminary experiments which have to be confirmed. Afterwards, we tried another dielectric material, namely a TiO_2 thin film deposited on glass substrate as illustrated in Figure 5.1. The incoming intensity at the glass/TiO_2 interface was measured at 55° incidence angle ($\theta_1(\omega)$, in Figure 2.5) for P-in P-out polarization orientations. As in shown in Figure 5.2, this structure gave also low SHG intensity but slightly higher than the glass/air interface.

Following that, we continued experimenting with different silicon wafers and simulated the SHG model in MATLAB. Then, we used a more complex material which is silicon-on-insulator (SOI) to compare the experimental results of silicon wafers. Finally, we observed some parameters which affect the SHG intensity and also found some crucial results which support the SHG method is an effective characterization method for semiconductor materials:

- The SHG signal strongly depends on the polarization states of the incident light and second harmonic light. For this experiment, Si(100) with thermal and native oxide were used. The maximum SHG intensities were measured in P-in P-out polarization states. In addition, the SHG intensity observed near zero for the S-out polarized SHG signal (such as P-in S-out and S-in S-out). This was expected results according to theoretical assumptions, because the surface isotropic contribution is near zero at S-out polarization states. It was verified also in rotational-anisotropy SHG experiments. Also, the maximum value for S- and P-out polarized SHG intensity is observed about 50° for both of them. In addition, when comparing results of both silicon wafers obtained SHG intensity, the native oxide one has a strongest SHG intensity. This is due to the different thickness of the oxide type.
- Additionally, we used the phenomenological surface SHG model to find the element ratios of the second order nonlinear susceptibility (χ_{zzz}/χ_{zii} and χ_{izi}/χ_{zii}). These ratios are different for each material. We determined different ratios for Si(100) with thermal and native oxide. It is shown that the SHG model gives a good agreement between the theory and experiment in Figure 4.4 and Figure 4.5.

- The angle of incidence light is also another critical parameter to determine the SHG intensity. Additionally, it is linked to the reflectivity coefficients of mediums. We measured the SHG intensity as a function of angle of incidence for Si(100) with thermal and native oxide. For the thermal oxide one, we observed the maximum SHG intensity at 52°. However, the results for the Si(100) with native oxide were different than the Si(100) with native oxide for P-in P-out polarization state because we couldn't observed any maximum incidence angle for SHG intensity between the angle of 25° and 65°. This is directly related to the polarization states of second harmonic and fundamental light. For example, in S-in P-out state, the maximum SHG intensity was found at 50° for Si(100) native oxide.
- Due to the separation of the electrons at silicon interface, the dc electric field arises inside the medium. It is a third order process and an additional effect to SHG intensity, called EFISH. To observe this effect of dc electric field, Si(100) with native and thermal oxide were measured at a given time. We observed that the SHG intensity for the thermal oxide does not change during the experiment whereas the native one increases. This difference is because of the charge separation of electron and holes, and it can give information about charge saturation at the interface of semiconductors. In addition, it is also possible to use this method to estimate the direction of the electric field due to the charge separation.
- When we rotated the samples, different SHG intensity values were observed at each azimuthal angle. This is directly related to the crystal orientation of sample. In the experimental results, for silicon with (100) crystal orientation, the S-out SHG intensity varies as a function of azimuthal angle with eightfold symmetry. However, if the surface contribution is greater than the bulk contribution such as for P-polarized SHG intensity, it was observed fourfold symmetry. To show this differences between bulk and surface contributions, we found the Fourier coefficients which describes the crystal facial orientations of the total SHG. These coefficients give information about the surface and bulk contributions. For Si(100) with thermal and native oxide, the isotropic surface contribution is dominant the other terms in P-in P-out state. However, in the case of P-in S-out, the anisotropic bulk contribution is dominant the other terms.

- After getting some information about Si wafers, we continued to investigate silicon on insulator (SOI). We compared the SHG intensity of ISLAND and BOX regions of SOI. ISLAND region has larger SHG intensity than BOX region, it is because of the multiple interfaces. We can examine the SHG intensity of ISLAND and BOX regions as a function of azimuthal angle. According to the results, the shape of graphs is same with Si(100) wafer which we used before. We again observed fourfold symmetry for P-polarized SHG intensity and eightfold symmetry for S-polarized SHG intensity. In addition, we measured SHG intensity with and without bias in time. This results show us the direction of the dc electric field inside, which arises from the charge separation at the interface, can be estimated by looking the time dependency of SHG intensity.

Consequently, the SHG model is a powerful tool for characterize the quality of the dielectric materials in microelectronic industry. In this study, it showed that this method allows us to identify and study on the surface and bulk of sample.

REFERENCES

Aktsipetrov, O. A., Fedyanin, A. A., Dadap, J. I., & Downer, M. C. (1996). Dc-electric-field-induced second-harmonic generation studies of surfaces and buried interfaces of column IV semiconductors. *Lasers Physics, 6*(6), 1142-1151.

Aktsipetrov, O. A., Mishina, E. D., & Petukhov, A. V. (1983). Electric-field-induced reflection in silver accompanying generation of the giant second harmonic. *Journal of Experimental and Theoretical Physics Letters, 37*(12), 707-708.

Alles, M. L., Pasternak, R., Lu, X., Tolk, N. H., Schrimpf, R. D., Fleetwood, D. M., Standley, R. W. (2007). Second harmonic generation for noninvasive metrology of Silicon-on-Insulator wafers. *IEEE Transactions on Semiconductor Manufacturing, 20*(2), 107-113.

Bloch, J., Mihaychuk, J. G., & Van Driel, H. M. (1996). Electron Photoinjection from Silicon to Ultrathin SiO2 Films via Ambient Oxygen. *Physical Review Letters, 77*(5), 920-923.

Bloch, J., Mihaychuk, J. G., Liu, Y., & Van Driel, H. M. (1995). Time-dependent second-harmonic generation from the Si–SiO2 interface induced by charge transfer. *Optics Letter, 20*(20), 2063-2065.

Bloembergen, N., & Pershan, P. (1962). Light waves at boundary of nonlinear media. *Physical Review, 128*(2), 606-622.

Bloembergen, N., Chang, R. K., Jha, S. S., & Lee, C. H. (1968). Optical second-harmonic generation in reflection from media with inversion symmetry. *Physical Review, 174*(3), 813-822.

Bottomley, D. J., Lüpke, G., Mihaychuk, J. G., & Driel, H. M. (1993). Determination of the crystallographic orientation of cubic media to high resolution using optical harmonic generation. *Journal of Applied Physics, 74*(10), 6072-6078.

Boyd, R. W. (2007). Nonlinear Optics. (Third ed.).

Chen, C. K., Castro, A. R., & Shen, Y. R. (1981). Surface-enhanced second-harmonic generation. *Physical Review Letters, 46*(2), 145-148.

Cundiff, S. T., Knox, W. H., Baumann, F. H., Evans-Lutterodt, K. W., & Green, M. L. (1998). Second-harmonic generation at the interface between Si(100) and thin SiO 2 layers. *Journal of Vacuum Science & Technology A, 16*, 1730-1733.

Dadap, J. I., Doris, B., Deng, Q., Downer, M. C., Lowell, J. K., & Diebold, A. C. (1994). Randomly oriented Angstrom-scale microroughness at the Si(100)/SiO2 interface probed by optical second harmonic generation. *Applied Physics Letters, 64*(16), 2139-2141.

Dadap, J. I., Hu, X. F., Russell, N. M., Ekerdt, J. G., & Lowell, J. K. (1995). Analysis of second-harmonic generation by unamplified, high-repetition-rate, ultrashort laser pulses at Si(100) interfaces. *IEEE Journal of Selected Topics in Quantum Electronics, 1*(1), 1145-1155.

Damianos, D., Pirro, L., Soylu, G., Ionica, I., Nguyen, V., Vitrant, G., Cristoloveanu, S. (2016). Second harmonic generation for contactless non-destructive characterization of silicon on insulator wafers. *Solid-State Electronics*, *115*(Part B), 237-243.

FemtoMetrix. Retrieved from www.femtometrix.com

Franken, P., Hill, A., Peters, C., & Weinreich, G. (1961). Generation of optical harmonics. *Physical Review Letters, 7*(4), 118-119.

Gielis, J. J., Gevers, P. M., Aarts, I. M., & Van de Sanden, M. C. (2008). Optical second-harmonic generation in thin film systems. *Journal of Vacuum Science & Technology A, 26*(6), 1519-1537.

Govorkov, S. V., Korteev, N. I., Petrov, G. I., Shumay, I. L., & Yakovlev, V. V. (1990). Laser nonlinear-optical probing of silicon/SiO2 interfaces: Surface stress formation and relaxation. *Applied Physics A, 50*(4), 439-443.

Heinz, T. F. (1982). Nonlinear optics of surfaces and adsorbates, *PhD thesis, University of California*

Ionica, I., Pirro, L., Nguyen, V., Kaminski, A., Vitrant, G., Onestas, L., Kryger, M. (2015). Second harmonic generation for non-destructive characterization of silicon-on-insulator substrates. *2015 Joint International EUROSOI Workshop and International Conference on Ultimate Integration on Silicon*, 185-188

Jun, B., Schrimpf, R. D., Fleetwood, D. M., White, Y. V., Pasternak, R., Rashkeev, S. N., Tolk, N. H. (2004). Charge trapping in irradiated SOI wafers measured by second harmonic generation. *IEEE Transactions on Nuclear Science, 51*(6), 3231-3237.

Kajikawa, K., Takezoe, H., & Fukuda, A. (1991). Symmetry and second-order susceptibility of hemicyanine monolayer studied by surface second-harmonic generation. *Japanese Journal of Applied Physics, 30*(5), 1050-1062.

Kwon, J. (2006). Second-harmonic generation and reflectance-anisotropy spectroscopy of vicinal Si(001). *PhD thesis, University of Texas at Austin*.

Lee, C. H., Chang, R. K., & Bloembergen, N. (1967). Nonlinear Electroreflectance in Silicon and Silver. *Physical Review Letters, 18*, 167-170.

Luppi, E., Hübener, H., & Véniard, V. (2010). Ab initio second-order nonlinear optics in solids: Second-harmonic generation spectroscopy from time-dependent density-functional theory. *Physical Review B, 82*(23), 235201.

Lüpke, G. (1999). Characterization of semiconductor interfaces by second-harmonic generation. *Surface Science Reports, 35*(3), 75-161.

Lüpke, G., Bottomley, D. J., & Van Driel, H. M. (1993). SiO2/Si interfacial structure on vicinal Si(100) studied with second harmonic generation. *Physical Review B, 47*(16), 10389-10394.

Lüpke, G., Bottomley, D. J., & van Driel, H. M. (1994). Second- and third-harmonic generation from cubic centrosymmetric crystals with vicinal faces: phenomenological theory and experiment. *Journal of the Optical Society of America B, 11*(1), 33-44.

Marka, Z., Singh, S. K., Wang, W., Lee, S. C., Kavich, J., Glebov, B., Tolk, N. H. (2000). Characterization of X-ray radiation damage in Si/SiO2 structures using second-harmonic generation. *IEEE Transactions on Nuclear Science, 47*(6), 2256-2261.

Mizrahi, V., & Sipe, J. (1988). Phenomenological threatment of surface second-harmonic generation. *Journal of the Optical Society of America B, 5*(3), 660-667.

Nguyen, V. H. (2014). Characterization of Silicon-On-Insulator through second-harmonic generation. *Internship Report, IMEP-LAHC, Grenoble/France*.

Palik, E. D. (1997). Handbook of Optical Constants of Solids .

Park, H. (2010). Second harmonic generation in Si/SiO2 system. *PhD thesis, Vanderbilt University*.

Park, H., Qi, J., Xu, Y., Lüpke, G., & Tolk, N. (2011). Polarization-dependent temporal behaviour of second harmonic generation in Si/SiO2 systems. *Journal of Optics, 13*, 0055202.

Park, H., Qi, J., Xu, Y., Varga, K., Weiss, S. M., Rogers, B. R., Tolk, N. (2009). Characterization of boron charge traps at the interface of Si/SiO2 using second harmonic generation. *Applied Physics Letters, 95*, 062102.

Pasternak, R., Shirokaya, Y. V., Marka, Z., Miller, J. K., Rashkeev, S. N., Pantelides, S. T., Fleetwood, D. M. (2003). Laser detection of radiation enhanced electron transport in ultra-thin oxides. *Nuclear Instruments and Methods in Physics Research, A*(514), 150-155.

Shen, Y. R. (2002). Principle of Nonlinear Optics.

Shriever, C., Bohley, C., Schilling, J., & Wehrspohn, R. B. (2010). Strain dependence of second-harmonic generation in silicon. *Optics Letters, 35*(3), 273-275.

Sipe, J. E. (1987, April). New Green-function Formalism for Surface Optics. *Journal of the Optical Society of America B, 4*(4), 481-498.

Sipe, J. E., Moss, D. J., & Van Driel, H. M. (1987). Phenomenological theory of optical second- and third-harmonic generation from cubic centrosymmetric crystals. *Physical Review B, 35*(3), 1129-1141.

Tom, H. W., Heinz, T. F., & Shen, Y. R. (1983). Second-harmonic reflection from silicon surfaces and its relation to structural symmetry. *Physical Review Letters, 51*(21), 1983-1986.

Wang, C. C., & Duminski, A. N. (1968). Second-harmonic generation of light at the boundary of alkali halides and glasses. *Physical Review Letters, 20*(13), 668-671.

Wang, W., Lüpke, G., Ventra, M. D., Pantelides, S. T., Gilligan, J. M., Tolk, N. H., Lucovsky, G. (1998). Coupled Electron-Hole Dynamics at the Si/SiO2 Interface. *Physical Review Letters, 81*(19), 4224-4227.

APPENDIX A

MACROSCOPIC MAXWELL'S EQUATION

The four vectors**,** the electric field **E**, the electric displacement field **D**, the magnetic field intensity **H**, the magnetic field **B**, in the macroscopic Maxwell's equations Equation (2.15) convert to the stationary continuous wave form. It exemplifies by Sipe (Sipe, 1987)

$$\begin{aligned} f(\mathbf{r},t) &= f(\mathbf{r})e^{-i\omega t} + c.c. \\ &= 2\mathrm{Re}\left[f(\boldsymbol{r})e^{-i\omega t}\right] \end{aligned} \tag{A.1}$$

Therefore,

$$\mathbf{D}(\mathbf{r})e^{-i\omega t} = \epsilon\,\mathbf{E}(\mathbf{r})e^{-i\omega t} \tag{A.2a}$$

$$\mathbf{H}(\mathbf{r})\boldsymbol{e^{-i\omega t}} = \mu^{-1}\mathbf{B}(\mathbf{r})e^{-i\omega t} \tag{A.2b}$$

The first Equation (2.15a) and third Equation (2.15c) of the macroscopic Maxwell's equation can be found easily $\boldsymbol{\nabla}\cdot\mathbf{E}(\mathbf{r}) = 0$ and $\boldsymbol{\nabla}\cdot\mathbf{B}(\mathbf{r}) = 0$, respectively. The second Equation (2.15b) is calculated and found

$$\begin{aligned} c\boldsymbol{\nabla}\times\mu^{-1}\mathbf{B}(\mathbf{r})e^{-i\omega t} - \epsilon\,\mathbf{E}(\mathbf{r})\frac{\boldsymbol{\partial}}{\boldsymbol{\partial t}}e^{-i\omega t} &= 0 \\ \boldsymbol{\nabla}\times\mathbf{B}(\mathbf{r}) - i\frac{\omega}{c}\epsilon\mu\,\mathbf{E}(\mathbf{r}) &= 0 \end{aligned} \tag{A.3}$$

The last one Equation (2.15d) is derived to

$$\begin{aligned} c\boldsymbol{\nabla}\times\mathbf{E}(\mathbf{r})e^{-i\omega t} + \mathbf{B}(\mathbf{r})\frac{\boldsymbol{\partial}}{\boldsymbol{\partial t}}e^{-i\omega t} &= 0 \\ \boldsymbol{\nabla}\times\mathbf{E}(\mathbf{r}) + i\frac{\omega}{c}\mathbf{B}(\mathbf{r}) &= 0 \end{aligned} \tag{A.4}$$

APPENDIX B

INHOMOGENEOUS MAXWELL EQUATION

We restore the electric displacement field $\mathbf{D}(\mathbf{r})$ when the polarization $\mathbf{P}(\mathbf{r}) \neq 0$. Therefore, it is calculated as Equation (2.18a)

$$\begin{aligned}\mathbf{D}(\mathbf{r}) &= \mathbf{E}(\mathbf{r}) + 4\pi\mathbf{P_t}(\mathbf{r}) \\ &= \mathbf{E}(\mathbf{r}) + 4\pi(\chi_e^{(1)}\mathbf{E}(\mathbf{r}) + \mathbf{P}(\mathbf{r})) \\ &= \mathbf{E}(\mathbf{r})(\mathbf{1} + 4\pi\chi_e^{(1)}) + 4\pi\chi_e^{(1)}\mathbf{P}(\mathbf{r}) \\ &= \epsilon\mathbf{E}(\mathbf{r}) + 4\pi\chi_e^{(1)}\mathbf{P}(\mathbf{r})\end{aligned} \tag{B.1}$$

The new version of the displacement electric field $\mathbf{D}(\mathbf{r})$ influences on the homogeneous Maxwell's equations just for $\boldsymbol{\nabla}\cdot\mathbf{D} = 0$ Equation (2.15a) and $c\boldsymbol{\nabla}\times\mathbf{H} - \dot{\mathbf{D}} = 0$ Equation (2.15b). Therefore, the first one can be described in this form:

$$\begin{aligned}\boldsymbol{\nabla}\cdot(\epsilon\mathbf{E}(\mathbf{r}) + 4\pi\chi_e^{(1)}\mathbf{P}(\mathbf{r})) &= 0 \\ \frac{\boldsymbol{\nabla}\cdot\epsilon\mathbf{E}(\mathbf{r})}{\epsilon} &= -\frac{4\pi\chi_e^{(1)}}{\epsilon}\boldsymbol{\nabla}\cdot\mathbf{P}(\mathbf{r}) \\ \boldsymbol{\nabla}\cdot\mathbf{E}(\mathbf{r}) &= -4\pi\epsilon^{-1}\boldsymbol{\nabla}\cdot\mathbf{P}(\mathbf{r})\end{aligned} \tag{B.2}$$

The other one can be found

$$\begin{aligned}c\boldsymbol{\nabla}\times\mu^{-1}\mathbf{B}(\mathbf{r})e^{-i\omega t} - (\epsilon\mathbf{E}(\mathbf{r}) + 4\pi\chi_e^{(1)}\mathbf{P}(\mathbf{r}))\frac{\boldsymbol{\partial}}{\boldsymbol{\partial t}}e^{-i\omega t} &= 0 \\ \frac{c\boldsymbol{\nabla}\times\mu^{-1}\mathbf{B}(\mathbf{r})e^{-i\omega t}}{c\mu^{-1}e^{-i\omega t}} - \frac{i\omega(\epsilon\mathbf{E}(\mathbf{r}) + 4\pi\chi_e^{(1)}\mathbf{P}(\mathbf{r}))}{c\mu^{-1}e^{-i\omega t}}e^{-i\omega t} &= 0 \\ \boldsymbol{\nabla}\times\mathbf{B}(\mathbf{r}) + i\tilde{\omega}\epsilon\mu\mathbf{E}(\mathbf{r}) &= -4\pi i\tilde{\omega}\mu\mathbf{P}(\mathbf{r})\end{aligned} \tag{B.3}$$

APPENDIX C

CALCULATION OF S- AND P- POLARIZED ELECTRIC FIELD DEPENDING ON PHENOMENOLOGICAL SURFACE SHG MODEL

To determine the s- and p-polarization components of the electric field, the curl equations in Equation 2.24, which are the second and fourth Maxwell inhomogeneous equations, are just considered. Firstly, we start with the fourth one Equation (2.24d). So, we put the total electric field $\mathbf{E}(\mathbf{r})$ and $\mathbf{B}(\mathbf{r})$ into $\boldsymbol{\nabla} \times \mathbf{E}(\mathbf{r}) - i\tilde{\omega}\mathbf{B}(\mathbf{r}) = 0$.

$$\begin{aligned}\boldsymbol{\nabla} \times [\mathbf{E}_{+}(\mathbf{r}) \exp(-i\omega z_o)\, h(z - z_o) + \mathbf{E}_{-}(\mathbf{r}) \exp(i\omega z_o)\, h(z_o - z) \\ + \boldsymbol{\xi}\delta(z - z_o) \exp(i\kappa \cdot \boldsymbol{R})] - i\tilde{\omega}[\mathbf{B}_{+}(\mathbf{r}) \exp(-i\omega z_o)\, h(z - z_o) \\ + \mathbf{B}_{-}(\mathbf{r}) \exp(i\omega z_o)\, h(z_o - z)] = 0\end{aligned} \tag{C.1}$$

To solve this equation, the following statements are used:

- The vector product rule:

$$\nabla \times f\vec{A} = (\nabla f) \times \vec{A} + f \cdot \left(\nabla \times \vec{A}\right) \tag{C.2}$$

- The derivative form of the step function and the Dirac delta:

$$\begin{aligned}\nabla h(z - z_o) &= \hat{z}\delta(z - z_o) \\ \nabla\delta(z - z_o) &= \hat{z}\delta'(z - z_o)\end{aligned} \tag{C.3}$$

- The special case for the step function:

$$h(z_o - z) = 1 - h(z - z_o) \tag{C.4}$$

Therefore, Equation (C.1) turn into

$$\boldsymbol{\nabla} \times h(z-z_o)[\mathbf{E}_+(\mathbf{r})\exp(-i\omega z_o) - \mathbf{E}_-(\mathbf{r})\exp(i\omega z_o)] + \nabla$$
$$\times \mathbf{E}_-(\mathbf{r})\exp(i\omega z_o) + \nabla \times \boldsymbol{\xi}\delta(z-z_o)\exp(i\boldsymbol{\kappa}\cdot\boldsymbol{R}) - i\tilde{\omega}[\mathbf{B}_+(\mathbf{r})$$
$$\exp(-i\omega z_o)\,h(z-z_o) + \mathbf{B}_-(\mathbf{r})\exp(i\omega z_o)\,h(z_o-z)] = 0 \qquad \text{(C.5)}$$

Then, it follows that

$$\boldsymbol{\nabla} h(z-z_o) \times [\mathbf{E}_+(\mathbf{r})\exp(-i\omega z_o) - \mathbf{E}_-(\mathbf{r})\exp(i\omega z_o)]$$
$$+h(z-z_o)[\nabla \times \mathbf{E}_+(\mathbf{r})\exp(-i\omega z_o) - \boldsymbol{\nabla} \times \mathbf{E}_-(\mathbf{r})\exp(i\omega z_o)]$$
$$+\nabla \times \mathbf{E}_-(\mathbf{r})\exp(i\omega z_o) + \left[\left(\nabla\delta(z-z_o)\right) \times \boldsymbol{\xi}\exp(i\boldsymbol{\kappa}\cdot\mathbf{R})\right]$$
$$+\delta(z-z_o)[\nabla \times \boldsymbol{\xi}\exp(i\boldsymbol{\kappa}\cdot\mathbf{R})] - i\tilde{\omega}[\mathbf{B}_+(\mathbf{r})\exp(-i\omega z_o)\,h(z-z_o)$$
$$+\mathbf{B}_-(\mathbf{r})\exp(i\omega z_o)\,h(z_o-z)] = 0 \qquad \text{(C.6)}$$

Using $\boldsymbol{\nabla} \times \mathbf{E}(\mathbf{r}) = i\tilde{\omega}\mathbf{B}(\mathbf{r})$, the equation changes to

$$\delta(z-z_o)\hat{z} \times [\mathbf{E}_+(\mathbf{r})\exp(-i\omega z_o) - \mathbf{E}_-(\mathbf{r})\exp(i\omega z_o)]$$
$$+h(z-z_o)[i\tilde{\omega}\mathbf{B}_+(\mathbf{r})\exp(-i\omega z_o) - i\tilde{\omega}\mathbf{B}_-(\mathbf{r})\exp(i\omega z_o)]$$
$$+i\tilde{\omega}\mathbf{B}_-(\mathbf{r})\exp(i\omega z_o) + [\hat{z} \times \boldsymbol{\xi}\,\delta'(z-z_o)\exp(i\boldsymbol{\kappa}\cdot\boldsymbol{R})$$
$$+\delta(z-z_o)(i\boldsymbol{\kappa} \times \boldsymbol{\xi})\exp(i\boldsymbol{\kappa}\cdot\mathbf{R})] - i\tilde{\omega}[\mathbf{B}_+(\mathbf{r})\exp(-i\omega z_o)\,h(z-z_o)$$
$$+\mathbf{B}_-(\mathbf{r})\exp(i\omega z_o)\,h(z_o-z)] = 0 \qquad \text{(C.7)}$$

Lastly, the equation is found at $z_o = 0^+$ and $\mathbf{R} = 0$

$$\delta(z-z_o)\hat{z} \times [\mathbf{E}_+(\mathbf{r}) - \mathbf{E}_-(\mathbf{r})] + \hat{z} \times \boldsymbol{\xi}\delta'(z-z_o) + \delta(z-z_o)(i\boldsymbol{\kappa} \times \boldsymbol{\xi}) = 0 \qquad \text{(C.8)}$$

We put $\mathbf{E}_\mp(\mathbf{r}) = (E_{s\mp}\hat{s} + E_{p\mp}\hat{p}_\mp)$ into the equation and also calculated

$$\delta(z-z_o)\hat{z} \times \left[(E_{s+}\hat{s} + E_{p+}\hat{p}_+) - (E_{s-}\hat{s} + E_{p-}\hat{p}_-)\right] + \hat{z} \times \boldsymbol{\xi}\delta'(z-z_o)$$
$$+\delta(z-z_o)(i\boldsymbol{\kappa} \times \boldsymbol{\xi}) = 0 \qquad \text{(C.9)}$$

To equal the equation zero, the different orders should be zero, such as there is no δ' term in the equation, so necessarily $\hat{z} \times \boldsymbol{\xi} = 0$. Therefore, we can find, $\xi_s = \xi_\kappa = 0$. The equation turns into

$$\hat{z} \times \left[(E_{s+}\hat{s} + E_{p+}\hat{p}_+) - (E_{s-}\hat{s} + E_{p-}\hat{p}_-)\right] + (i\kappa\hat{\kappa} \times \xi_z\hat{z}) = 0 \qquad \text{(C.10)}$$

We examine the special case when $\hat{\kappa} = \hat{x}$

$$\left[E_{s+}(\hat{z} \times \hat{s}) + E_{p+}(\hat{z} \times \hat{p}_+)\right] - [E_{s-}(\hat{z} \times \hat{s}) + E_{p-}(\hat{z} \times \hat{p}_-)]$$

$$+i\kappa\xi_z(\hat{\kappa} \times \hat{z}) = 0 \qquad \text{(C.11)}$$

Using the vector product rule in Equation C.2, we separate above equation into the vector coordinates $\hat{s}$ and $\hat{\kappa}$ respectively (because there is no $\hat{z}$ component):

$$E_{p+} + E_{p-} + i\kappa v w^{-1}\xi_z = 0 \qquad \text{(C.12)}$$

$$E_{s+} - E_{s-} = 0$$

Next we will use the second equation of inhomogeneous Maxwell's equations Equation (2.24b) $\boldsymbol{\nabla} \times \mathbf{B}(\mathbf{r}) + i\tilde{\omega}\epsilon\mu\mathbf{E}(\mathbf{r}) = -4\pi i\tilde{\omega}\mu\mathbf{P}(\mathbf{r})$ and we put the total electric field $\mathbf{E}(\mathbf{r})$ and $\mathbf{B}(\mathbf{r})$ into the equation

$$\boldsymbol{\nabla} \times [\mathbf{B}_+(\mathbf{r}) \exp(-i\omega z_o)\, h(z - z_o) + \mathbf{B}_-(\mathbf{r}) \exp(i\omega z_o)\, h(z_o - z)]$$

$$+i\tilde{\omega}\epsilon\mu[\mathbf{E}_+(\mathbf{r}) \exp(-i\omega z_o)\, h(z - z_o) + \mathbf{E}_-(\mathbf{r}) \exp(i\omega z_o)\, h(z_o - z)$$

$$+\boldsymbol{\xi}\delta(z - z_o) \exp(i\kappa \cdot \boldsymbol{R})] = -4\pi i\tilde{\omega}\mu[P\delta(z - z_o) \exp(i\boldsymbol{\kappa} \cdot \mathbf{R})] \qquad \text{(C.13)}$$

Using same arguments like before one, the above equation turns into

$$\delta(z-z_o)\hat{z}\times[\mathbf{B}_+(\mathbf{r})\exp(-i\omega z_o)+\mathbf{B}_-(\mathbf{r})\exp(i\omega z_o)]$$

$$-i\tilde{\omega}\epsilon\mu[\mathbf{E}_+(\mathbf{r})\exp(-i\omega z_o)\,h(z-z_o)+\mathbf{E}_-(\mathbf{r})\exp(i\omega z_o)\,h(z_o-z)]$$

$$+i\tilde{\omega}\epsilon\mu[\mathbf{E}_+(\mathbf{r})\exp(-i\omega z_o)\,h(z-z_o)+\mathbf{E}_-(\mathbf{r})\exp(i\omega z_o)\,h(z_o-z)]$$

$$+i\tilde{\omega}\epsilon\mu\boldsymbol{\xi}\delta(z-z_o)\exp(i\kappa\cdot\boldsymbol{R})=-4\pi i\tilde{\omega}\mu[P\delta(z-z_o)\exp(i\boldsymbol{\kappa}\cdot\mathbf{R})] \quad \text{(C.14)}$$

Then,

$$\delta(z-z_o)\hat{z}\times[\mathbf{B}_+(\mathbf{r})\exp(-i\omega z_o)+\mathbf{B}_-(\mathbf{r})\exp(i\omega z_o)]$$

$$+i\tilde{\omega}\epsilon\mu\boldsymbol{\xi}\delta(z-z_o)\exp(i\kappa\cdot\boldsymbol{R})=-4\pi i\tilde{\omega}\mu[P\delta(z-z_o)\exp(i\boldsymbol{\kappa}\cdot\mathbf{R})] \quad \text{(C.15)}$$

We put $\mathbf{B}_{\mp}(\mathbf{r})=\sqrt{\mu\epsilon}(E_{p\mp}\hat{s}\pm E_{s\mp}\hat{p}_{\mp})$ into the equation and do the calculation at $z_o=0^+$ and $\mathbf{R}=0$,

$$\hat{z}\times\left[\sqrt{\mu\epsilon}\left(E_{p+}\hat{s}-E_{s+}\hat{p}_+\right)+\sqrt{\mu\epsilon}\left(E_{p-}\hat{s}-E_{s-}\hat{p}_-\right)\right]+i\tilde{\omega}\epsilon\mu\xi_z\hat{z}$$

$$=-4\pi i\tilde{\omega}\mu P \quad \text{(C.16)}$$

After,

$$\sqrt{\mu\epsilon}(\hat{z}\times\hat{s})E_{p+}-\sqrt{\mu\epsilon}(\hat{z}\times\hat{p}_+)E_{s+}+\sqrt{\mu\epsilon}(\hat{z}\times\hat{s})E_{p-}-\sqrt{\mu\epsilon}(\hat{z}$$

$$\times\hat{p}_-)E_{s-}+i\tilde{\omega}\epsilon\mu\xi_z\hat{z}=-4\pi i\tilde{\omega}\mu(P_s\hat{s}+P_\kappa\hat{\kappa}+P_z\hat{z}) \quad \text{(C.17)}$$

We separate the equation the vector field $\hat{s}$, $\hat{\kappa}$ and $\hat{z}$ respectively

$$E_{s+}+E_{s-}=4\pi i\tilde{\omega}^2\mu w^{-1}P_s$$

$$E_{p+}-E_{p-}=-4\pi i\tilde{\omega}\mu\sqrt{\mu\epsilon}^{-1}P_\kappa$$

$$\xi_z=-4\pi\epsilon^{-1}P_z \quad \text{(C.18)}$$

Finally, we can find the components of the electric field with respect to $\hat{s}_{\pm}$ and $\hat{p}_{\pm}$ using Equation C.12 and Equation C.18

$$E_{s\pm} = \frac{2\pi i\tilde{\omega}^2}{w}\hat{s}\cdot P$$
$$E_{p\pm} = \frac{2\pi i\tilde{\omega}^2}{w}\hat{p}_{\pm}\cdot P \qquad \text{(C.19)}$$